Alma Mater Studiorum – Università di Bologna

School of Science
Department of Physics and Astronomy
Master Degree Programme in Astrophysics and Cosmology

A gamma-ray beam scenario to mimic giant radio galaxies: an investigation with cosmological MHD simulations

Graduation Thesis

Presented by:
Valerio Tritapepe

Supervisor:
Chiar.mo Prof. Franco Vazza

Academic year 2024-2025
Graduation date V

Abstract

Giant Radio Galaxies (GRG) are among the most extended structures in the Universe and are powered by supermassive black holes. Recent observations, in particular the discovery of the 7-Megaparsec long radio galaxy Porphyrion, challenge the standard interpretation of these systems as classical relativistic jets, given the large energetic demands, the apparent lack of interaction with the external medium, the absence of significant precession of their supermassive black hole, and their remarkable stability against magnetohydrodynamical instabilities.

In this Thesis, I have quantitatively tested the viability of a recently proposed alternative scenario to overcome some of the aforementioned difficulties: the γ-ray beam model, in which the observed radio emission may be produced by secondary electron–positron pairs injected by high energy photons as they propagate through an intergalactic magnetic field, while interacting with the extragalactic background light. To investigate this mechanism, I developed new Julia-based numerical routines to model the propagation and radiative properties of γ-ray beams within realistic intergalactic environments, extracted from recent cosmological MHD simulations produced with the Enzo code.

By statistically sampling thousands of trajectories across different redshift, I derived the expected distributions of jet sizes and compared them with the observed population of GRGs, while also predicting the corresponding radio and γ-ray luminosities and evaluating their detectability with LOFAR and Fermi-LAT.

My results suggest that a fraction of the most extended radio structures may arise from this mechanism, with important implications for the interpretation of GRGs and their contribution to the magnetisation of the cosmic web.

Contents

Abstract **i**

List of Figures **vi**

List of Tables **vii**

1 Introduction **1**

1.1 Radio Galaxies and AGN unification model 1

1.2 Review of AGN TeV γ-ray sources 4

1.3 Giant Radio Galaxies 6

1.3.1 Extreme Radio Galaxies: Porphyrion and similar sources 7

1.3.2 Open problems and theoretical conundrums 8

1.3.3 The γ-ray Beam Model for Porphyrion 9

1.3.4 Radiative processes for the γ-ray beam model 13

1.3.5 Radio galaxies and their connection with the study of the origin of cosmic magnetism 18

2 Methods **24**

2.1 Cosmological Enzo simulation 24

2.2 New numerical routines produced for this Thesis 30

2.2.1 Halo selection criteria 30

2.2.2 Modelling the trajectories of γ-ray beams from active galactic nuclei 31

2.2.3 Modelling of periodic boundary conditions 35

2.2.4 Definition and calculation of observable jet lengths 36

2.2.5 Generation of the observable statistics of γ-ray beams 37

2.2.6 Simulated maps of radio and γ-ray emission 39

2.2.7 Modelling the full-sky distributions of radio and γ-ray emission from γ-ray beams 41

3 Results **45**
3.1 Statistical properties of the simulated jets 45
3.1.1 Intrinsic distributions and projection effects 45
3.1.2 Cumulative statistics and comparison with GRG observations data 50
3.2 Predictions on the radio and γ-ray luminosity distributions of γ-ray beams 54

4 Discussion and Conclusions **60**
4.1 Methods and Results 61
4.2 Implications and future perspectives 63

A Appendix **67**

Bibliography **72**

List of Figures

1.1 Fanaroff-Riley classification 2
1.2 Schematic representation of Active Galactic Nuclei in the unified scheme 5
1.3 The giant radio galaxy Porphyrion observed with LOFAR. 8
1.4 Fermi-LAT countmaps of the region around Porphyrion 11
1.5 Spectral Energy Distribution of Porphyrion. 12
1.6 Spectral Energy Distribution for the extragalactic background light . . . 14
1.7 Schematic representation of synchrotron radiation 15
1.8 Schematic representation of inverse Compton scattering 17
1.9 Schematic representation of Faraday rotation 19

2.1 Observed trend of the RRM of polarized background sources 26
2.2 2D maps of projected mean baryonic density, DM density and magnetic field intensity 28
2.3 Mass distribution of halos 31
2.4 3D Distribution of baryonic density and massive halos 32
2.5 Physical properties along jet trajectories 33
2.6 Schematic representation of periodic boundary conditions 35
2.7 Cumulative largest linear sizes of known GRGs 40
2.8 2D maps of the jet environment and radiative properties 42

3.1 Distribution of jet lengths 46
3.2 Projection effects on jet length 48
3.3 Distribution of projected jet lengths 49
3.4 Normalized cumulative number density of the projected jet lengths . . . 51
3.5 Volume-weighted cumulative distributions of expected all-sky source counts 53
3.6 Predicted all-sky radio and γ-ray flux distributions 56
3.7 Predicted flux distributions binned by physical length 58
3.8 Predicted flux distributions binned by redshift 59

List of Tables

1.1 The unified model for radio-loud sources. 4

2.1 Simulation snapshots and their corresponding redshift 27
2.2 Number of halos for each redshift 30
2.3 Comoving shell volumes and weight factors for the five redshift range . . 39

3.1 Empirical scaling factors used for the observational calibration 52

1 Introduction

This Thesis concerns both the wide topic of the physics of (Giant) Radio Galaxies (GRG), as well as their connection with the origin of magnetism in the Universe. I will first provide a general definition of radio galaxies and of the AGN unified model (Sec. 1.1), followed by a review of gamma-ray emitting AGNs (Sec. 1.2). I will then delve into the extreme case of Porphyrion (Sec. 1.3.1), the most extended radio galaxy known to date, which poses a number of puzzles and theoretical conundrums (Sec. 1.3.2). Subsequently, I will present the γ-ray beam model, a new alternative model proposed to explain Porphyrion-like objects and bypass the many theoretical problems posed by this object (Sec. 1.3.3), along with the radiative processes necessary to sustain it (Sec. 1.3.4). Finally, I will explore how the physics of radio galaxies is connected to the origin of cosmic magnetism and its possible production scenarios, and how this Thesis work may contribute to the ongoing debate between primordial and astrophysical seeding model (Sec. 1.3.5).

1.1 Radio Galaxies and AGN unification model

Radio galaxies (RGs) and radio-loud quasars, collectively radio-loud AGN (RLAGN), are active galaxies characterized by radio emission driven by powerful, collimated outflows (jets) extending on scales from pc to Mpc. Their characteristic radio emission is synchrotron emission, indicating the presence of magnetic fields and highly relativistic electrons and/or positrons. The generation of these outflows likely occurs extremely close to the central supermassive black hole (SMBH) contained in the centre of the host galaxy. The mechanism for launching the jets is believed to be the Penrose/Blandford-Znajek process (Penrose, 1969; Blandford & Znajek, 1977), in which the accreted material transports magnetic field down to the event horizon of the black hole, where it can be twisted by the rotation of space-time close to the black hole. In this process, rotational energy is extracted from the black hole and converted into mechanical work that powers the relativistic jet. The energetics involved in these structures are huge: the lifetime-averaged jet kinetic power is in the range $10^{36} - 10^{40}$ W, and over their lifetimes, the total amount of injected energy may reach up to 10^{54} J or more for the most powerful sources (Hardcastle & Croston, 2020).

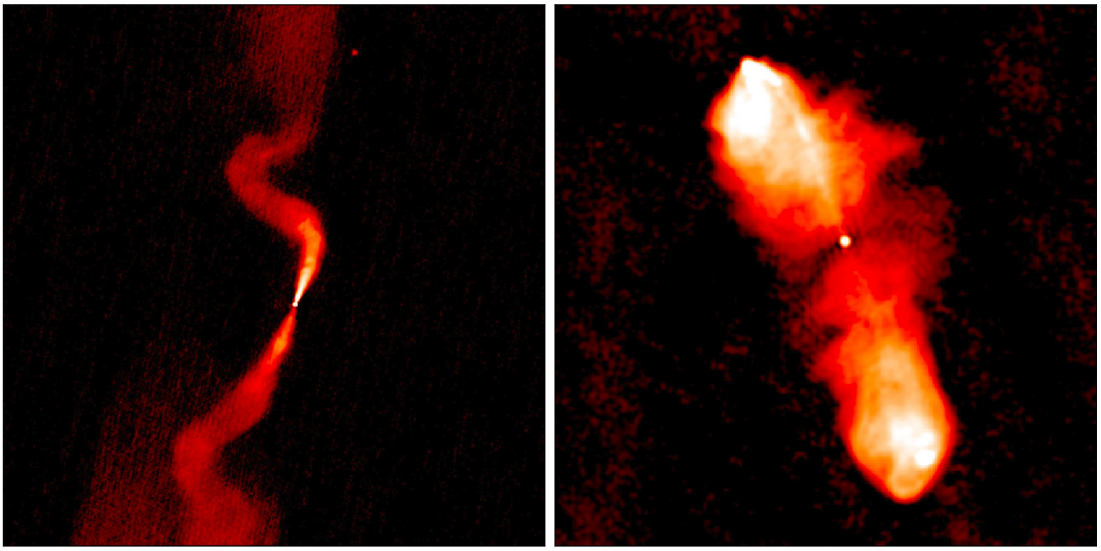

Figure 1.1. Radio images of nearby radio galaxies showing two different morphologies: the Fanaroff-Riley class I source 3C 31 (left) and the Fanaroff-Riley class II source 3C 98 (right). Image adapted from Hardcastle & Croston (2020).

These structures can be morphologically classified using the Fanaroff-Riley (FR) scheme (Fanaroff & Riley, 1974), which distinguishes objects based on their radio luminosity and jet dynamics: the edge-brightened FRII radio galaxies are thought to have jets that remain relativistic throughout, terminating in a hotspot (generated by internal shock), while the centre-brightened FRI radio galaxies have initially relativistic jets that decelerate already on kpc scales. Figure 1.1 shows representative examples of the two FR classes. This morphological distinction is also associated with a difference in radio power; indeed, FRI and FRII usually have a radio power respectively lower and higher than $10^{24.5}\,\mathrm{W\,Hz^{-1}}$ at a rest frame frequency of 1.4 GHz (e.g. Bicknell, 1995; Tchekhovskoy & Bromberg, 2016). It has to be noted that, as radio surveys have reached lower flux limits, evidence has also emerged that the FR morphological division is less closely tied to radio luminosity than previously thought, with the emergence of an unexpected population of low-luminosity sources with the FRII morphology (e.g. Capetti, A. et al., 2017; Mingo et al., 2019). Furthermore, the structural difference is a result of the interplay of jet power and environmental density. Jets of the same power might remain relativistic and well collimated in poor environments, but decelerate into diffuse plumes or tails and entrain gas as they interact with a rich surrounding intergalactic medium. Essentially, it is now believed that the FR dichotomy mainly reflects the dynamics of the jet and its interaction with the surrounding environment, rather than the intrinsic properties of the central engine or the growth mode.

Observations of the optical spectra of radio galaxy hosts reveal a broad diversity of spectroscopic properties. Some objects exhibit strong high-excitation broad and narrow emission lines, resembling those of Seyfert galaxies, whereas others show weak or no line emission. Following the classification introduced by Laing et al. (1994), this observational dichotomy has been divided into "low-excitation radio galaxies" (LERGs) and "high-excitation radio galaxies" (HERGs). The HERG population includes both "narrow-line radio galaxies" (NLRGs) and "broad-line radio galaxies" (BLRGs), whose optical spectra resemble those of classical Seyfert 2 and Seyfert 1 galaxies respectively, as well as optically selected quasars. The latter have spectra similar to those of BLRGs but are distinguished by a dominant optical continuum emission. While the FR scheme classifies the macroscopic structures of the RGs morphology, the differences in the optical spectra of active galaxies have historically been explained by an orientation-based unified model. For radio-quiet AGN, Antonucci (1993) explains the difference between type 1 and type 2 Seyfert galaxies in terms of an anisotropic obscuring structure, referred to as the "torus". This structure, plausibly surrounding the accretion flow, obscures the nuclear continuum and broad emission lines in objects where the observer's line of sight passes through it (type 2), but allows them to be seen directly from other lines of sight (type 1). In the case of radio-loud objects, the situation is further complicated by the presence of the jet, which provides a source of broad-band anisotropic radiation on all spatial scales, and by the existence of LERGs, which have no counterpart in the Seyfert 1/2 orientation-based scheme. Nevertheless, Barthel (1989) was able to develop the first successful orientation-based unified model for RLAGN, demonstrating that quasars and RGs are members of the same physical population. Subsequently, Hardcastle et al. (1998) extended this model to lower-redshift sources, unifying BLRGs and NLRGs. According to this scheme, a quasar or a BLRG is observed when the line of sight does not intercept the obscuring torus, whereas a NLRG is observed when the torus blocks the view of the centre. Finally, the most extreme manifestation of this geometric unification are the blazars, a sub-category of RLAGN characterized by bright variable emission at a range of wavelengths. Their extreme properties are not intrinsic but are the result of relativistic Doppler boosting effects, which occur when the relativistic jet is oriented at a small angle to the line of sight, pointing almost directly toward the observer.

The orientation-based model is incomplete because it does not account for LERGs. It was proposed that the missing narrow emission lines were completely obscured or that emitting material was absent, but mid-IR and X-ray properties ruled out this possibility (e.g. Chiaberge et al., 2002; Hardcastle et al., 2009). This fact established

that the difference between HERGs and LERGs is not just an effect of the observer's viewing angle, but resides in the physics governing the central engine, that is, the radiative efficiency of the accretion flow. The modern view separates radio-loud AGN into two distinct accretion regimes: radiatively inefficient (RI) and radiatively efficient (RE). Accretion disks capable of generating more than a few per cent of the Eddington luminosity,

$$L_{\rm Edd} = \frac{4\pi G M_{\rm BH} c m_p}{\sigma_T}\,, \tag{1.1}$$

are radiatively efficient and can produce the optical luminosity observed in HERGs. In contrast, LERGs operate at much lower Eddington-scaled accretion rates and are therefore radiatively inefficient (Hardcastle & Croston, 2020). In radiatively inefficient AGN, the accretion flow releases most of its energy in mechanical form through relativistic jets rather than as electromagnetic radiation. The modern comprehensive AGN unification scheme synthesizes orientation, accretion mode, and jet power in a comprehensive scheme for RLAGN. In this framework, an object's classification depends on two independent parameters: accretion efficiency (RI vs. RE) and orientation to the line of sight. The unified model for RLAGN is summarized in Table 1.1 and shown in a schematic visual representation in Figure 1.2.

Table 1.1. The unified model for radio-loud sources.

	Jet at large angles to line of sight	**Intermediate angles**	**Jet closely aligned to line of sight**
Radiatively inefficient (RI)	Low-excitation radio galaxy, LERG (FRI or FRII)	Low-excitation radio galaxy, LERG (FRI or FRII)	BL Lac object
Radiatively efficient (RE)	Narrow-line radio galaxy, NLRG (some FRI, mostly FRII)	Broad-line radio galaxy, BLRG, or lobe-dominated or steep-spectrum quasar (some FRI, mostly FRII)	Core-dominated, flat-spectrum or OVV quasar

1.2 Review of AGN TeV γ-ray sources

AGN hosting relativistic jets represent the most powerful and ubiquitous particle accelerators in the Universe. When these jets are closely aligned with the line of sight, the sources are observed as blazars, and their non-thermal emission dominates the extragalactic γ-ray sky. Observations at TeV energies have shown that most of the AGN detected in this band belong to the high-frequency end of the blazar population, in particular to high-frequency-peaked BL Lac objects (HBLs). Within this group,

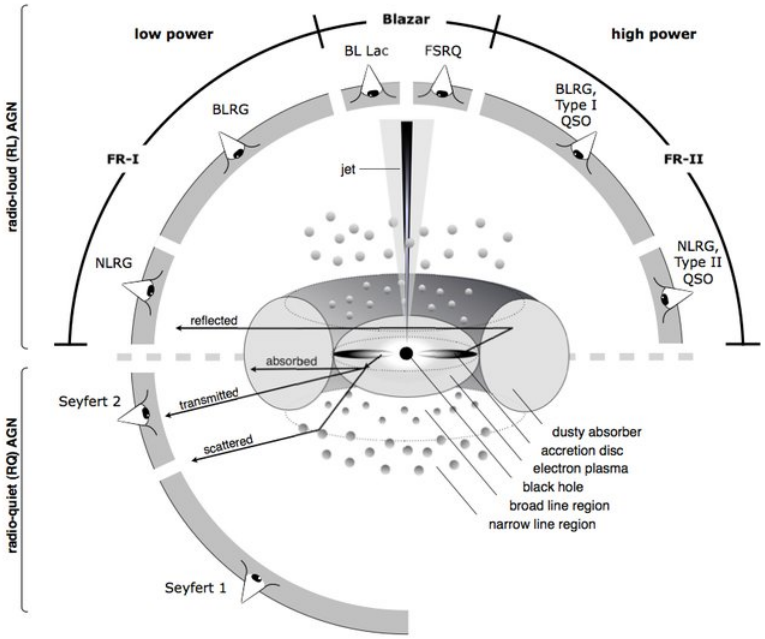

Figure 1.2. Schematic representation of our understanding of the AGN phenomenon in the unified scheme. The type of object we see depends on the viewing angle, whether or not the AGN produces a significant jet emission, and how powerful the central engine is. Graphic by Marie-Luise Menzel, adopted from Beckmann & Shrader (2013)

increasing attention has recently been devoted to the so-called extreme blazars, which represent the most energetic systems of this class (Biteau et al., 2020).

Their spectral energy distributions (SEDs) display two broad components. The first hump, peaking at infrared to X-ray wavelengths, is commonly explained as synchrotron emission from electrons accelerated in the jet. The second hump, peaking above MeV energies, is often attributed to inverse Compton scattering (e.g. Tavecchio et al., 2010).

The first firm detections of TeV photons from AGN were obtained in the late 1990s, through observations of flaring activity in nearby BL Lac objects such as Mkn 501. In particular, BeppoSAX observations during the 1997 outburst revealed a synchrotron peak extending to unusually high energies (Pian et al., 1997), demonstrating that relativistic jets can accelerate particles to energies sufficient to produce TeV γ-rays. Subsequent X-ray studies further highlighted the existence of sources with extremely high synchrotron peak frequencies (Costamante, L. et al., 2001).

A major step forward occurred in the mid-2000s with the operation of new-generation imaging atmospheric Cherenkov telescopes. Observations with H.E.S.S. revealed blazars with very hard intrinsic spectra, with their γ-ray peak located above $\sim$ 1–3 TeV. Shortly

afterwards, sources such as 1ES 0229+200 were found to emit γ-rays up to energies of at least ~ 10 TeV with remarkably hard spectra, establishing the class of extreme-TeV blazars (Aharonian et al., 2006). More recent observations with current Cherenkov arrays have further extended the detected emission from some nearby blazars to energies of several tens of TeV, confirming that AGN jets can sustain particle acceleration to extremely high energies (see review in Biteau et al., 2020).

Extreme blazars represent the most energetic tail of the HBL population. They can be broadly divided into two categories. Extreme synchrotron sources show a synchrotron peak energy $h\bar{\nu}_{\rm x} \geq 1\,{\rm keV}$, while extreme-TeV sources have a γ-ray peak energy $h\bar{\nu}_{\gamma} \geq 1\,{\rm TeV}$. Extreme-synchrotron sources represent only a small fraction of the HBL population, highlighting the rarity of objects capable of sustaining such high particle energies (Biteau et al., 2020). Although these two definitions are related, they do not always coincide from the observational viewpoint. Indeed, extreme behaviour can manifest in different ways, with some sources showing extreme synchrotron peaks and others displaying persistent hard TeV spectra. As discussed by Biteau et al. (2020), because of their hard spectra and emission extending to multi-TeV energies, these objects constitute a key population for studying the most efficient particle acceleration processes in relativistic jets and for probing the propagation of very high-energy γ-rays through the intergalactic medium.

1.3 Giant Radio Galaxies

Giant radio galaxies (GRG) are members of a rare RG subpopulation which attain megaparsec-scale proper lengths. They are usually defined as radio sources with a projected linear size larger than 0.7 Mpc. Because the conversion between angular length and projected proper length depends on cosmological parameters, which remain uncertain, it is not always clear whether a given observed RG satisfies the GRG definition. The first objects of this type to be found were 3C236 and DA240, identified by Willis et al. (1974), and since this first pioneering discovery, these relatively rare sources have been growing in number due to the all-sky surveys and to the increasing amount of sensitive and good quality radio and optical data. Recently, Mostert et al. (2024) have catalogued 11 485 unique GRGs. How the extraordinary sizes of GRGs are reached is still poorly understood, and it is possible that a combination of different factors may be responsible for each specific source. A recent review by Dabhade et al. (2023) suggests that an interplay of three primary factors may be responsible. First, GRGs may be powered by exceptionally powerful and long-lived AGN activity, capable of

producing jets that propagate at such large distances. However, GRGs are seen over a wide range of jet powers and their SMBH masses do not differ from the corresponding distributions of normal-sized RGs. This suggests that they do not necessarily have a more powerful AGN (Dabhade et al. 2020a). Second, their growth could result from recurrent or episodic jet activity, where multiple cycles of outbursts extend the lobes over time. Nevertheless, observational evidence suggests that only a small fraction of GRGs are known to exhibit evidence of recurrent activity (5.1% and 5.8% respectively, in Dabhade et al. 2020b and Dabhade et al. 2020a). Third, GRGs are often found in relatively low-density environments, where the reduced external pressure allows jets to propagate farther without significant disruption. However, different studies have shown (e.g., Dabhade et al. 2020b, Andernach & Brüggen 2025) that at least 10-20% of GRGs reside in centres of galaxy clusters as brightest cluster galaxy.

1.3.1 Extreme Radio Galaxies: Porphyrion and similar sources

Recently, the sample of GRGs has become large enough to study even the extreme end of the GRG size distribution, and new record-breaking objects have been added to this sample. Based on the association between detected objects in the LOFAR Two-Metre Sky Survey (LoTSS) and Optical sources, (Hardcastle et al. 2023), the largest radio source ever found was reported, with a largest linear size (LLS) of 6.9 Mpc (Oei et al., 2024). Named after a giant from greek mythology, Porphyrion consists of a northern lobe, a northern jet, a core, a southern jet with an inner hotspot, and a southern outer hotspot with a backflow, as can be seen from Figure 1.3. Even if there are some doubts about the correct host and host redshift, in Oei et al. (2024) these outflows have been associated with a massive (i.e. stellar mass of $M_\star = 6.7^{+1.4}_{-1.4} \cdot 10^{11} M_\odot$) galaxy, with a measured spectroscopic redshift of $z = 0.896 \pm 0.001$. The sky-projected length is $L_\mathrm{p} = 6.43 \pm 0.05$ Mpc, but the actual full length may exceed this number as it depends on the unknown inclination angle of the jets with respect to the sky plane. It has been estimated to be $L_\mathrm{Porph} \sim 7$ Mpc (physical). According to the model, the jet had an average power of $P \sim 10^{46}$ erg s^{-1} and an age of $\tau \sim 1.9$ Gyr, with an average expansion speed of the outflow of v = 0.012c.

Although it is the largest, Porphyrion is not the only object with extreme dimensions. Andernach & Brüggen (2025) examined the properties of a larger sample of GRGs, in particular selecting those with LLS larger than 3 Mpc. The sample comprises 143 GRGs, including 6 larger than 5 Mpc, which corresponds to about 1% of all known GRGs larger than 0.7 Mpc. Upon first inspection, no single GRG appeared to conform to an FR I morphology on both sides, and only nine displayed lobes deviating from the FR II type.

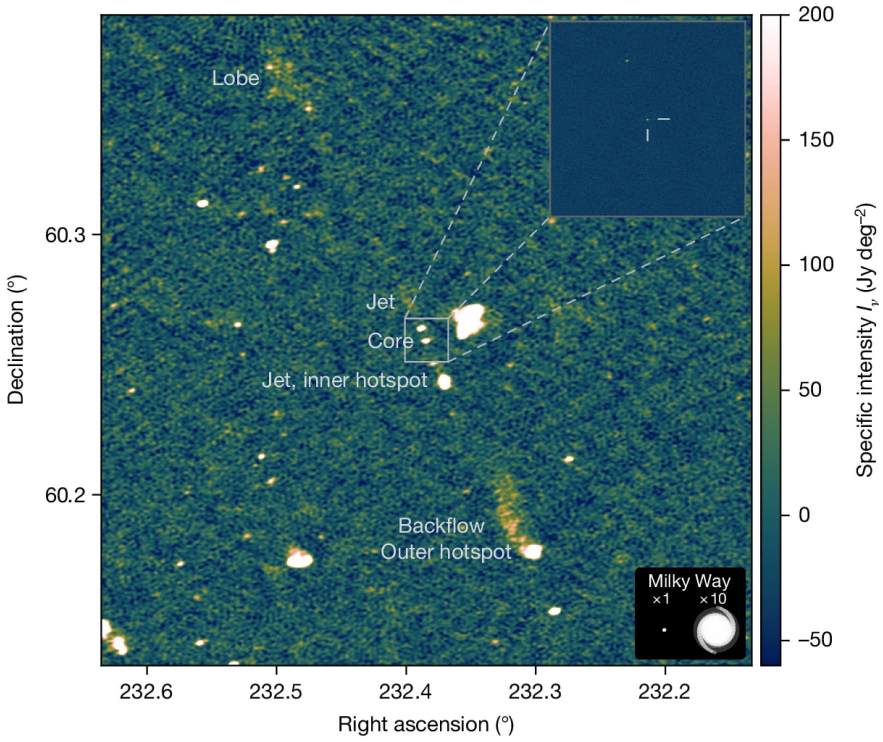

Figure 1.3. Deep radio image of the 7 Mpc-long giant radio galaxy Porphyrion observed at $\lambda = 2.08$ m (144 MHz) with the International LOFAR Telescope (ILT). The inset shows high-resolution VLBI imagery of the central core. This structure represents the largest black hole-driven outflow known to date. Image adapted from Oei et al. (2024).

Furthermore, it is observed that the shorter lobe is most often the brighter one. This is likely to arise from the fact that the lobe interacting with a denser environment exerts more work against the medium, leading to a more efficient conversion of jet energy into radio emission. Simultaneously, by propagating through a denser ambient medium, the lobe encounters a larger resistance and it tends to be shorter, mirroring the standard asymmetry found in typical radio galaxies.

1.3.2 Open problems and theoretical conundrums

The existence of objects like Porphyrion challenges our understanding of jet physics. If Porphyrion is assumed to be the extreme case of the known phenomenology of moving radio plasma jets, several physical anomalies arise:

- **The Energy Budget Problem:** Considering its radio power and age, the total energy deposited by Porphyrion's jets is $\sim 8 \cdot 10^{62}$ erg. In order to power such outflows, the central SMBH must have undergone a substantial mass growth in

the past, and must have accreted $\Delta M_{BH} = 2\frac{E}{c^2} = 9^{+2}_{-1} \cdot 10^8 M_\odot$ (Oei et al., 2024). This value is so problematic that it exceeds the estimated mass of one of the two possible hosts of Porphyrion in this region, i.e. a quasar with mass $M_q \sim 2 \cdot 10^8 M_\odot$, making the association with Porphyrion impossible. Furthermore, the accretion of such large masses is typically associated with mergers, which induce large velocity dispersion: one would therefore expect disturbed morphologies of the host galaxy, which are instead not observed.

- **The Stability Problem:** The SMBH jets remain collimated over several mega-parsecs. This contradicts theoretical predictions and simulations of shorter jets (Perucho, 2019), where magnetohydrodynamical (MHD) instabilities - mainly Kelvin-Helmholtz instabilities - disrupt the flow. The straightness of the lobes suggests anomalously low peculiar velocities ($v_p < 100$ km/s), implying that the hosts may reside at the bottom of local gravitational potential wells, possibly surrounded by voids.

- **High-redshift challenges:** The fact that 19 GRGs (13% of the sample with LLS > 3 Mpc) are found at $z \geq 1$ challenges our understanding of how such structures could grow to these sizes given the denser conditions of the early Universe and the stronger inverse Compton (IC) cooling from the Cosmic Microwave Background (CMB), which would further decrease the radiative life-time of the synchrotron-emitting electrons.

1.3.3 The γ-ray Beam Model for Porphyrion

As an attempt to circumvent most of the open problems outlined above, recently Neronov et al. (2025) have proposed an intriguing alternative explanation for the formation of Porphyrion and other similar objects, which might alleviate several theoretical puzzles. The idea is that the observed jet-like structure is not made out of plasma, but is produced by a beam of very high-energy γ-rays (as in AGN TeV sources, see Sec.1.2), producing electron positron pairs in the Intergalactic medium (IGM). These secondary pairs are deposited along the beam and may produce synchrotron and inverse Compton emission. Such γ-ray beams do not, therefore, transport charged particle plasma from the AGN nucleus out to the radio emitting lobes, nor do they need to sustain their own magnetic fields in order to be observable. The electrons and positrons are continuously injected by the conversion of γ-ray photons as they propagate along a very narrow emission cone, and they get visible in the radio domain only whenever their conversion into electron-positron pairs happen in the presence of a large enough intergalactic magnetic

field.

We will now deeply explore this model, to better understand the physics underlying it and the advantages and implications that this interpretation offers for Porphyrion and other similar objects. In this framework, the radio emission observed from Porphyrion is interpreted as synchrotron radiation emitted by the secondary electron-positron pairs produced by a beam of very high-energy γ-rays, specifically in the TeV energy range ($E_{\gamma_0} \gtrsim 10$ TeV). Narrow beams of photons with energies exceeding 10 TeV are emitted by the population of "TeV blazars", which has been observed by Biteau et al. (2020). Through the interaction with the visible/infrared Extragalactic Background Light (EBL), these photons deposit their energy into the IGM by creating electron-positron pairs, which then cool down and emit the observed radio synchrotron radiation. If a sizeable magnetic field is present in the environment crossed by the beam, then the emission resulting from pairs may be powerful enough to be detectable. Assuming a magnetic field strength typical of the large-scale structure (LSS), $B \sim 10\,\mathrm{nG}$, the electrons responsible for the observed radio frequencies

$$\nu_s \simeq 100 \left[\frac{B}{10\mathrm{nG}}\right] \left[\frac{E_e}{30\mathrm{GeV}}\right]^2 \mathrm{MHz}\,, \tag{1.2}$$

(~ 100 MHz) must possess energies in the range of $E_e \simeq 10 - 100$ GeV. These same relativistic electrons will interact with the Cosmic Microwave Background through the inverse Compton process, up-scattering the CMB seed photons to γ-ray energies. The ratio of the bolometric IC Flux (F_{IC}) to the bolometric Synchrotron flux (F_{syn}) is proportional to the ratio of the energy densities of the CMB ($U_{CMB} \propto (1+z)^4$) and of the magnetic field (U_B)

$$\frac{F_{\mathrm{IC}}}{F_{\mathrm{syn}}} = \frac{U_{\mathrm{CMB}}}{U_{\mathrm{B}}}\,. \tag{1.3}$$

Since U_{CMB} is fixed by cosmology at the source redshift, and $F_{syn} \sim 10^{-16}\,\mathrm{erg\,cm^{-2}\,s}$ is known from radio observation, the expected IC flux depends on the local magnetic field strength. Specifically, a weaker magnetic field implies a lower U_B, which in turn predicts a much higher, potentially observable, γ-ray flux. By analyzing data from the Fermi-LAT telescope, Neronov et al. (2025) reported that no significant detection of Porphyrion has been found in the MeV-GeV band, as shown in the countmaps of the Porphyrion region in Figure 1.4. The non-detection of the source imposes an upper limit on the γ-ray flux, which is represented by the gray-shaded region in Figure 1.5. By modeling the synchrotron and IC emission assuming a cutoff power-law distribution of electrons, it becomes evident that a magnetic field lower than 30 nG (e.g., the dashed

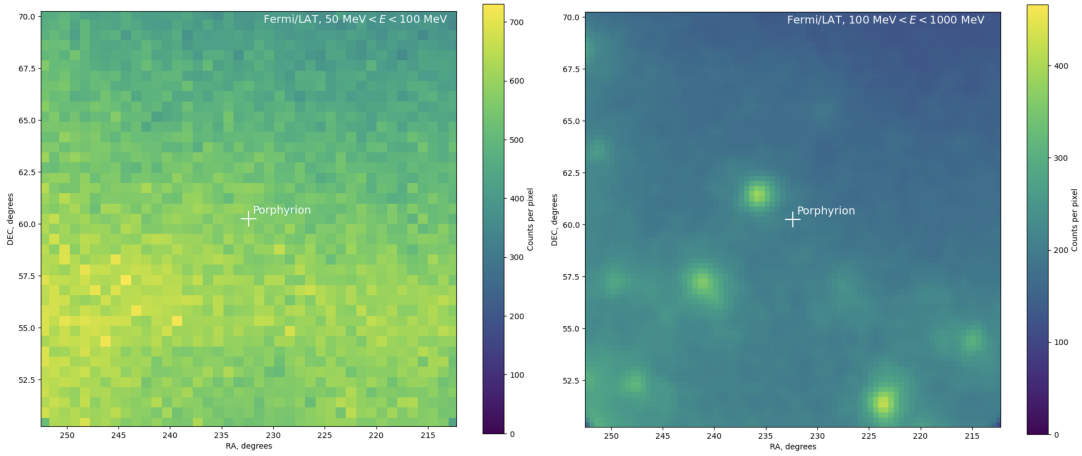

Figure 1.4. Fermi-LAT countmaps of the region around Porphyrion in the energy ranges $50\,\mathrm{MeV} < E_\gamma < 100\,\mathrm{MeV}$ (left) and $100\,\mathrm{MeV} < E_\gamma < 1000\,\mathrm{MeV}$ (right). The size of the Porphyrion source is smaller than the size of the cross at the source position. The brighter spots in the right image are sources other than Porphyrion detected by Fermi-LAT. Image reproduced from Neronov et al. (2025).

curve corresponding to 15 nG) would result in an IC flux exceeding the Fermi-LAT sensitivity limits. Consequently, this observation sets a lower bound on the magnetic field strength of the emitting region of $B_{\mathrm{min}} \simeq 30\,\mathrm{nG}$. This corresponds to a comoving minimal magnetic field strength of:

$$B_{\mathrm{min,comoving}} = \frac{B_{\mathrm{min}}}{(1+z)^2} \simeq 8\ \mathrm{nG}\,, \tag{1.4}$$

at the redshift of the source.

This γ-ray beam model offers a solution to the conundrums posed by the standard plasma jet interpretation:

1. **Solution to the Energy Budget**: The standard model implies an immense energy deposition of $\sim 8 \cdot 10^{62}\,\mathrm{erg}$ and a total accreted mass ($\Delta M \sim 10^9 M_\odot$) exceeding the mass of the host black hole. The γ-ray model significantly reduces these energetic demands. The structure could be the remnant trace of a short period of high activity (at least ~ 10 Myr, the time needed for γ-rays to propagate over the jet length), and Neronov et al. (2025) estimate that the total energy of the γ-ray beam to explain the observed radio emission should have been $\leq 3 \cdot 10^{61}\,\mathrm{erg}$, approximately 30 times lower than the standard scenario, making possible the host association with Porphyrion.

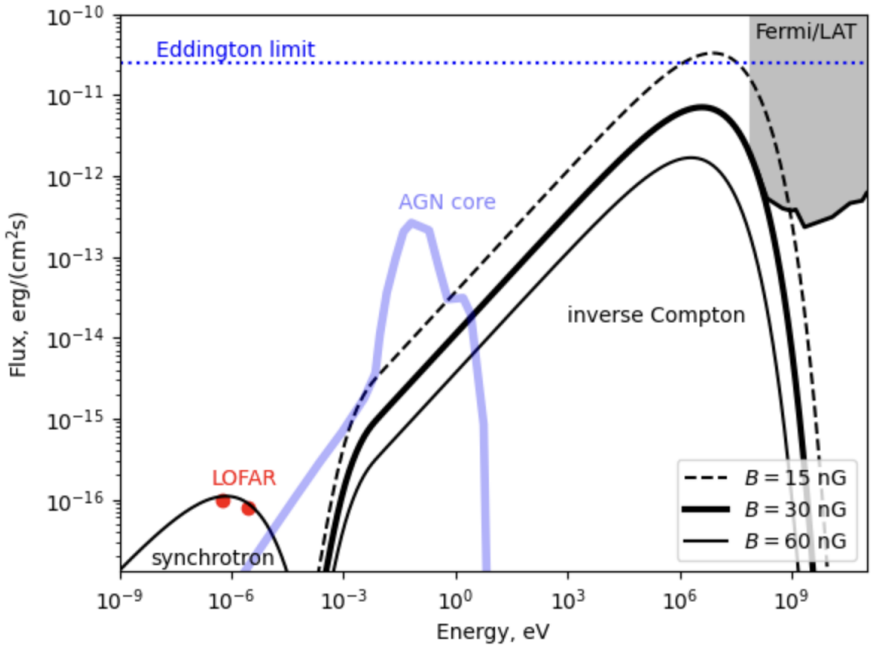

Figure 1.5. Spectral Energy Distribution of Porphyrion modelled as synchrotron and inverse Compton emission. The gray-shaded region indicates the upper limit on γ-ray flux derived from Fermi-LAT non-detection. The light blue curve represents the host AGN spectral energy distribution model from Oei et al. (2024). The dashed horizontal line shows the level of flux expected from a source powered by a $10^9\,M_\odot$ black hole emitting at Eddington limit. The curves corresponding to different magnetic field strengths ($B = 15$ nG, dashed; $B = 30$ nG, thick solid; and $B = 60$ nG, thin solid) show the expected IC flux. The red points give the observed flux at radio wavelengths. Image reproduced from Neronov et al. (2025).

2. **Solution to the stability problem**: The exceptional straightness of Porphyrion over 7 Mpc is naturally explained. While in the standard scenario the jets require fine-tuned parameters to maintain MHD stability, the γ-ray beam model completely bypasses the problem. The jet-like structure, defined by the propagation of high-energy photons, naturally produces a straight trajectory limited only by the mean free path (D_{γ_0}) of the γ-rays through the EBL. At redshift $z \sim 1$, the mean free path is estimated to be $D_{\gamma_0} \simeq 10$ Mpc for energies of $E_{\gamma_0} = 10$ TeV, and decreases to ~ 1 Mpc for $E_{\gamma_0} = 30$ TeV (Fitoussi et al., 2017). This range is comparable to the observed length scale of Porphyrion.

3. **Relaxation of environmental requirements:** Finally, the standard model requires propagation of jets into low density environment like cosmic voids to avoid resistance, while this condition is not required for the γ-ray model. Furthermore,

the magnetic field strength derived from the non-detection of γ-rays in Porphyrion is close to the global estimate of the magnetic field in the filaments of the LSS (e.g. Carretti et al., 2025). This suggests that the jet may be contained within a filament of the LSS, which would provide the magnetic field necessary for the observed synchrotron emission.

While this model is overall plausible from the physical point of view, some of the parameters in the model were calibrated to reproduce the main properties of Porphyrion. In my Thesis I will for the first time test the statistical application of this model to a large cosmological volume, and compute in detail how often objects like Porphyrion may form, and what are the chances to observe them in the radio and in the γ-ray band.

1.3.4 Radiative processes for the γ-ray beam model

This section provides an overview of the radiative processes involved in the γ-ray beam model presented in this Thesis. I therefore discuss the pair production mechanism via interaction with the extragalactic background light and, subsequently, the cooling processes of the secondary particles through synchrotron emission and inverse Compton scattering.

Pair Production mechanism with the Extragalactic Background Light

The pair production is the process by which a neutral boson (typically a high-energy photon) creates a subatomic particle and its own antiparticle. For this transformation to happen, the process must follow fundamental conservation laws, including energy, linear momentum, angular momentum, and electric charge. In the context of this work, the most relevant mechanism is $\gamma - \gamma$ annihilation and subsequent pair production. This process occurs when high-energy photons of energy E interact with low-energy extragalactic background photons of energy ϵ, resulting in the creation of electron-positron pairs

$$\gamma_E + \gamma_\epsilon \rightarrow e^+ + e^-. \tag{1.5}$$

This reaction is energetically possible when the centre of mass energy of the two photon system exceeds the rest mass energy of the created pair ($2m_e c^2$). These background photons extend from the cosmic microwave background to the near-ultraviolet (UV) wavelengths. The UV/optical/infrared background radiation is called the extragalactic background light. Following Spurio (2018), the cross section for the pair-production

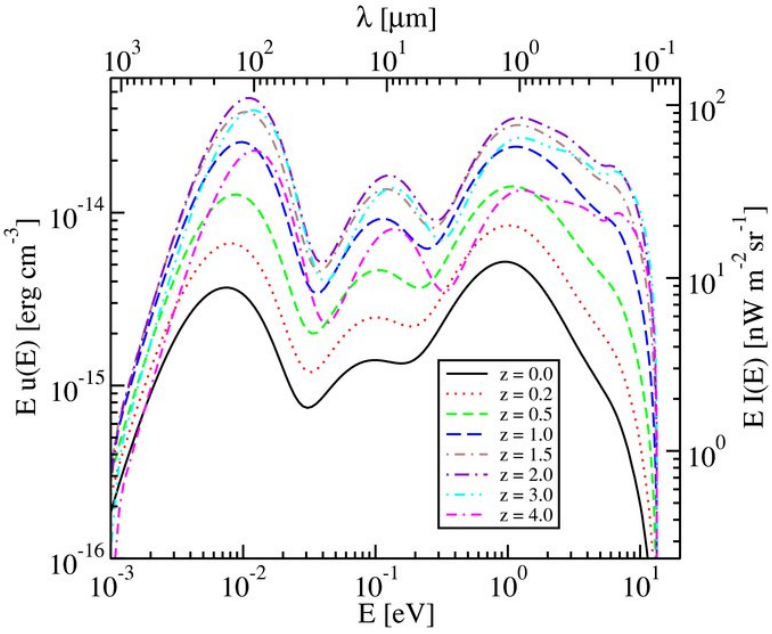

Figure 1.6. Spectral energy distribution for the extragalactic background light (EBL) energy density as a function of proper photon energy (bottom scale) or wavelength (upper scale) for different values of redshift. Image reproduced from Finke et al. (2010).

process is described by the Bethe-Heitler formula

$$\sigma(E,\epsilon) \simeq 1.25 \times 10^{-25}(1-\zeta^2)\,\mathrm{cm}^2, \tag{1.6}$$

where $\zeta = 1 - \frac{(m_e c^2)^2}{E\cdot\epsilon}$. The cross section in (1.6) is maximized when

$$\epsilon \simeq 2\frac{(m_e c^2)^2}{E} \simeq \frac{520\,\mathrm{GeV}}{E}\mathrm{eV}\,, \tag{1.7}$$

and the threshold energy is a factor of two lower.

The EBL is the totality of light emitted by stars, galaxies, and AGN since the birth of the Universe. Today, this pervasive photon background consists of light emitted at all epochs, modified by the redshift due to the expansion of the Universe. The bulk of the EBL falls within the range from $\sim 10^{-3}$ to 10 eV, corresponding to wavelengths from the far-infrared to the near-ultraviolet ($\sim 1000 - 0.1\,\mu$m). Figure 1.6 shows the estimated spectral energy distribution of the EBL as a function of photon energy or wavelength according to the model of Finke et al. (2010). In the UV, optical and near-IR, most of the EBL is due to direct starlight, as well as a subdominant contribution from AGN. From the mid-IR to submillimetric wavelengths, the EBL consists of re-emitted light

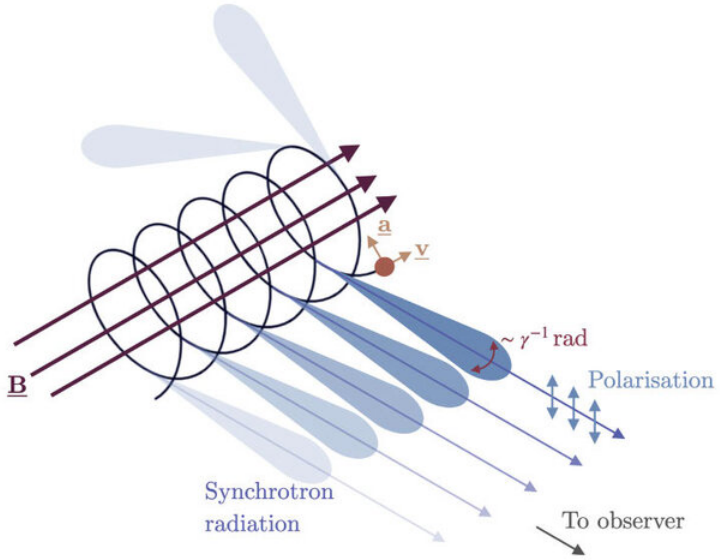

Figure 1.7. Schematic representation of synchrotron radiation from an ultra-relativistic electron. The particle spirals along a magnetic field line B with velocity v and acceleration a. Due to relativistic effects, the emitted radiation is strongly beamed into a narrow cone of angular width $\sim \gamma^{-1}$ along the instantaneous direction of motion. The resulting macroscopic emission is highly linearly polarized. Graphic by Emma Alexander.

from dust particles. The different lines in the figure represent the EBL background at different redshifts.

Synchrotron radiation

Synchrotron radiation is the electromagnetic radiation emitted by ultra-relativistic electrons accelerating in a magnetic field. The following summary is based on the theoretical framework presented by Longair (2011).

When an electron with charge e and mass m_e moves in a magnetic field B with a velocity v, it is subjected to the Lorentz force, which causes it to spiral around the magnetic field lines (as illustrated in Figure 1.7) In the ultra-relativistic limit ($\gamma \gg 1$, where γ is the Lorentz factor, defined as $\gamma = (1 - v^2/c^2)^{-1/2}$), the total power radiated by a single relativistic electron with a pitch angle α is given by:

$$-\left(\frac{dE}{dt}\right)_S = 2\sigma_T c U_{mag} \left(\frac{v}{c}\right)^2 \gamma^2 \sin^2 \alpha \,, \tag{1.8}$$

where $\sigma_T \approx 6.65 \times 10^{-25}$ cm^2 is the Thomson scattering cross-section, c is the speed of light, and $U_{mag} = B^2/2\mu_0$ is the energy density of the magnetic field. The distribution

of pitch angles for a population of high-energy electrons is expected to be isotropic, leading to an average energy loss rate

$$-\left(\frac{dE}{dt}\right)_S = \frac{4}{3}\sigma_T c U_{mag}\gamma^2 \,. \tag{1.9}$$

To evaluate the radiation spectrum for a distribution of electron energies, we have to consider that the spectra of non-thermal sources can often be represented by power-law spectra. Therefore, we study the emission spectrum for a power law-distribution of electron energies

$$N(E)\mathrm{d}E = kE^{-p}\mathrm{d}E \,, \tag{1.10}$$

where $N(E)\mathrm{d}E$ is the number density of electrons in the energy interval $E + \mathrm{d}E$ and k is a constant. The superposition of the spectra from these electrons results in a total emissivity expressed in terms of $k\,, B\,, \nu$ (frequency) and fundamental constants:

$$J(\nu) \propto kB^{(p+1)/2}\nu^{-(p-1)/2}. \tag{1.11}$$

Thus, the emitted spectrum, written as $J(\nu) \propto \nu^{-\alpha}$, where $\alpha = (p-1)/2$ is known as the spectral index, is determined by the slope of the electron energy spectrum p. The emissivity also depends upon the combination of quantities $kB^{\alpha+1}$. A distinct signature of synchrotron radiation is the high degree of polarization. For relativistic electrons, significant radiation is only observed if the trajectory of the electron lies within an angle $1/\gamma$ of the line of sight (depicted by the emission cones in Figure 1.7). The radiation from a single electron is elliptically polarised, however, because all elliptical contributions from a population of electrons cancel out, the resultant polarisation is linear. The fractional linear polarization is

$$\Pi = \frac{p+1}{p+\frac{7}{3}} \,. \tag{1.12}$$

Thus, for a typical value of $p = 2.5$, the fractional polarization of synchrotron radiation is expected to be about 72%. However, observed polarization is often lower due to disordered magnetic fields or Faraday rotation.

Inverse Compton scattering

The inverse Compton scattering is the process by which ultra-relativistic electrons scatter low energy photons up to higher energies, so that the photons gain energy at the expense of the kinetic energy of the electrons. The process is called inverse Compton scattering

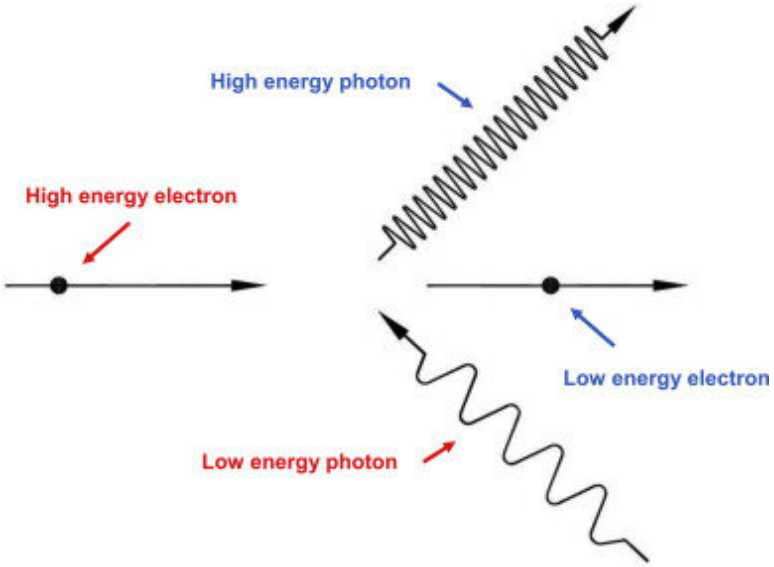

Figure 1.8. Schematic representation of the inverse Compton scattering process. A low-energy seed photon (longer wavelength) interacts with a high-energy relativistic electron. During the collision, the kinetic energy is transferred from the electron to the photon. The net result in the laboratory frame is a highly energetic up-scattered photon (shorter wavelength) and a decelerated electron. Image reproduced from Wright (2015).

because the electrons lose energy, rather than the photons. Following the derivation in Longair (2011), the process can be understood by considering the interaction in the rest frame of the relativistic electron. In this frame, the electron sees the background photons (which have frequency ν_0 in the laboratory frame) Doppler-shifted to a higher frequency $\nu' \approx \gamma\nu_0$. If the photon energy in this rest frame is low enough ($h\nu' \ll m_e c^2$), the interaction behaves as classical Thomson scattering, where the photon is scattered without loss of energy. When this scattered photon is transformed back into the laboratory frame, it undergoes another Doppler shift due to the electron's motion. The net result is that the frequency of the scattered photon, ν_{IC}, is increased by a factor of γ^2:

$$\nu_{IC} \approx \gamma^2 \nu_0 \,. \tag{1.13}$$

For example, an electron with $\gamma \sim 10^4$ can up-scatter a typical photon from the CMB ($\nu_0 \sim 10^{11}$ Hz) to the hard X-ray energies $\nu \sim 10^{19}$ Hz. This kinematic interaction and the resulting energy transfer are schematically depicted in Figure 1.8. The total energy lost by a relativistic electron via IC scattering is:

$$-\left(\frac{dE}{dt}\right)_{IC} = \frac{4}{3}\sigma_T c U_{rad} \left(\frac{v^2}{c^2}\right) \gamma^2 \,, \tag{1.14}$$

where U_{rad} is the energy density of radiation in the laboratory reference frame. Notice the remarkable similarity of (1.14) to the expression (1.9) for the mean energy loss rate of the ultra-relativistic electron by synchrotron radiation. This leads to the equivalence

$$\frac{U_{rad}}{U_B} = \frac{(dE/dt)_{IC}}{(dE/dt)_S} \,. \tag{1.15}$$

It is apparent that the IC scattering process is an effective means of creating very high-energy photons. It also becomes an inevitable drain of energy for high-energy electrons whenever they pass through a region in which there is a large energy density of radiation.

1.3.5 Radio galaxies and their connection with the study of the origin of cosmic magnetism

Magnetic fields are ubiquitous on all scales probed so far, from planets and stars to the large-scale magnetic fields detected in galaxies and galaxy clusters. The origin and evolution of these magnetic fields is the subject of intense study. While they are generally understood to be the amplified products of weak seed fields (e.g. Donnert et al., 2018), the source of these seeds remains unclear. They could either be primordial relics dating back to the CMB epoch, or astrophysical product injected into the IGM during galaxy formation through magnetised winds and jets.

Radio galaxies are a key class of objects, at the crossroad between galaxy evolution, cosmology, high-energy astrophysics and magnetism. Particularly relevant for my Thesis, they represent a powerful tool to investigate the origin of cosmic magnetism, serving as primary diagnostic probes for detecting magnetic fields in the intergalactic medium and also participating in the magnetisation of the universe through astrophysical seeding processes. The radio emission from astrophysical sources is mainly due to synchrotron radiation, so the investigation of cosmic magnetism is linked to the properties of this emission. Radio galaxies are the most prominent source of synchrotron radiation in the sky, often exhibiting high degrees of linear polarization. However, the observed polarization properties are rarely intrinsic: the Faraday rotation produced by the magnetised thermal plasma along the line of sight changes the polarization angle of a linearly polarized radiation as this travels through a magneto-ionic medium (free electrons in a magnetic field). This rotation occurs because the magnetised medium acts as a birefringent plasma, causing the two circularly polarized components of the radiation to propagate at different phase velocities. A schematic representation of this

effect is provided in Figure 1.9. Consequently, the rotation angle $\Delta\psi$ [rad] is directly proportional to the square of the observing wavelength λ [m]:

$$\Delta\psi = \mathrm{RM}\lambda^2\,. \tag{1.16}$$

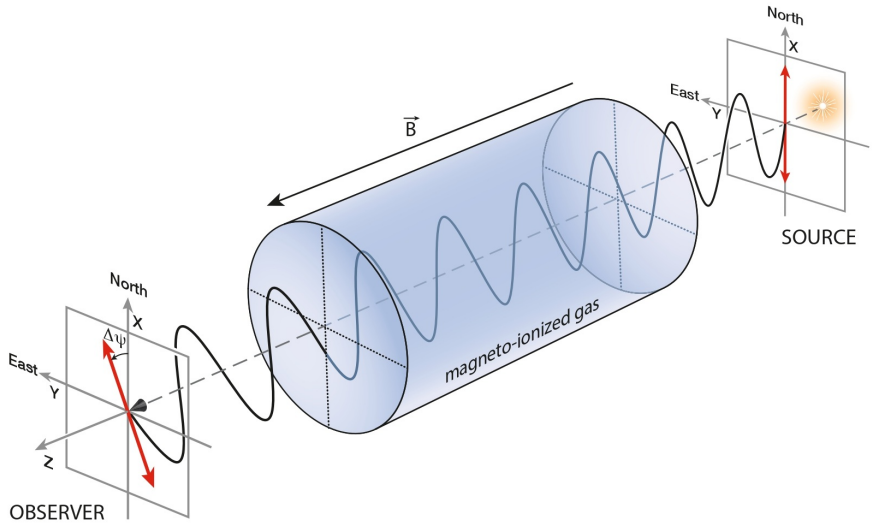

Figure 1.9. Schematic representation of Faraday rotation showing qualitatively how the electric field vector of a linearly polarized radio wave oscillates along the propagation direction, between the source (far side) and the observer (near side), and how the polarization orientation (red double-headed arrow) undergoes Faraday rotation as the wave passes through a magneto-ionized region (blue shaded cylinder). Image adapted from Ferrière et al. (2021).

The Faraday rotation measure (RM) is (e.g. Govoni, F. et al., 2010)

$$\mathrm{RM} = 0.812 \int_{\text{source}}^{0} \frac{n_e B_{\parallel}}{(1+z)^2} dl \quad \mathrm{rad\,m^{-2}}\,, \tag{1.17}$$

where z is the source redshift, the integration is performed from the source to the observer along the proper path length l [pc] on the sight line, n_e is the free-electron proper number density [$\mathrm{cm^{-3}}$], and $B_{\parallel}$ is the proper magnetic field along the line of sight [μG]. In general, the observed RM of an extragalactic source is the combination of several RM components along the sight line:

$$\mathrm{RM} = \mathrm{GRM} + \mathrm{RM}_{eg} + \mathrm{N}\,, \tag{1.18}$$

which comprises a galactic RM (GRM) component, an extragalactic term ($\mathrm{RM_{eg}}$), and

the noise N. To investigate the extragalactic component, the GRM has to be subtracted off, giving the Residual Rotation Measure (RRM):

$$\mathrm{RRM} = \mathrm{RM} - \mathrm{GRM}\,. \tag{1.19}$$

To extract the magnetic field strength from these observations, the degeneracy in the RM Equation (1.17) between $B_{\parallel}$ and n_e must be broken. Typically, this can be done once the thermal gas density distribution is inferred from X-ray observations of bremsstrahlung emission or the Sunyaev-Zel'dovich (SZ) effect. However, a number of complications can make the direct application of the RM equation inaccurate (Carretti & Vazza, 2025). First, the electron number density and the magnetic field are not necessarily perfectly correlated at all scales, particularly below the spatial resolution limits of observations or numerical simulations. Second, the analytical RM formulation assumes a relatively smooth and isotropic medium; applying it requires caution when the magnetic field is not perfectly isotropic, its components lack a Gaussian distribution, or when the gas exhibits large clumping factors, as often occurs in the multi-phase cores of galaxy clusters. Third, non-thermal particles can also contribute to the total observed Faraday rotation, introducing a potential bias if only thermal electrons are assumed. When accounting for all the aforementioned effects, this physical mechanism can be exploited for the radio galaxies, allowing to map the strength and structure of magnetic fields across a wide range of astrophysical environments. Magnetic field strengths in galaxy groups and clusters are typically measured using two distinct approaches: observing radio galaxies embedded directly within the group/cluster, or observing background radio galaxies whose line of sight passes through the group/cluster medium (Hardcastle & Croston, 2020). While studies of cluster-centre radio galaxies date back to the 1970s, the observation of background sources has more recently enabled the detailed mapping of cluster magnetic field distributions and the investigation of the relationships between these magnetic fields and the thermodynamic conditions of the cluster gas (e.g. Bonafede et al., 2010; Govoni, F. et al., 2010).

The full distribution of radio galaxies in the sky has the potential to provide 'Rotation Measure Grids'. By observing sufficiently many strongly polarized radio sources across the sky with current (LOFAR) and future (SKA) facilities, it will be possible to determine magnetic field structures on a range of scales and cosmic environments. These dense grids of background sources will enable detailed investigations into the intergalactic magnetic field within filaments of large-scale structures (O'Sullivan, S. P. et al., 2019).

Mini-review of primordial seeding models: basic concepts and indications from simulations

Primordial seeding models assume that "seed" magnetic fields were generated in the very early Universe, i.e. before the formation of any astrophysical objects (e.g. stars, galaxies, black holes). The physical mechanisms proposed in primordial models may take place during inflation, or in the post-inflationary epoch. In the first case, magnetic fields can be generated by breaking the conformal invariance for the electromagnetic field, or by coupling it to other light fields (e.g. Turner & Widrow, 1988; Fujita et al., 2015). Depending on the specific mechanisms, the resulting seed fields have different characteristics in terms of scales, spectral energy distribution and amplitudes. However, a key feature of inflationary models is that the generated seed magnetic field may be correlated on scales larger than the present-day cosmological horizon.

In the post-inflationary case, magnetic fields can be generated during phase transitions at critical cosmological epochs, i.e. during the electroweak phase transition, or during the quantum chromodynamics (QCD) phase transition (e.g. Quashnock et al., 1989; Ellis et al., 2019). Standard generation mechanisms for magnetic fields require first-order phase transition, which produce the nucleation, expansion, and collision of "bubbles" of a new phase within an old, metastable phase. First order phase transitions release latent heat and promote large density jumps and violent shock waves, which can source the generation of magnetic fields by inducing strong currents. However, first order phase transitions are generally disfavoured by our current theoretical understanding. There are also mechanisms that involve second-order perturbations, e.g. via the Harrison mechanism and recombination, but these can generate only very weak final fields (e.g. Fidler et al., 2016; Matarrese et al., 2005). For example, the Harrison mechanisms is a two fluid battery effect which might have occurred between the proton fluid and the tightly coupled electron-photon fluid. At the epoch of the matter-radiation equality ($z_{eq} \sim 3400$) the separately conserved angular momenta of the two fluid caused protons to spin down with expansion faster than electrons (which were still coupled to photons). Such difference in rotation might have leads to currents that induced magnetic fields, by an effect that is a second order perturbations of the fluid equations. However, Hutschenreuter et al. (2018) produced direct cosmological simulations of the Harrison mechanism, reporting only a seed magnetic field generation of order $\sim 10^{-29}$ G. A key property of all post-inflationary scenarios is that the generated seed magnetic fields must have correlations only on scales much smaller than the cosmological horizon.

A fundamental aspect of all primordial generation models is that the volume filling factor of their seed field is very large, i.e. namely 100% of the cosmic volume must have

a relic of the seed magnetic field. This appears consistent with the modelling of the lack of secondary inverse Compton emission at $\sim$ GeV energies around blazars, which is commonly interpreted as evidence for $\geq 10^{-17} - 10^{-16}$ G magnetic fields on ~ 100 Mpc scales, i.e. in cosmic voids (Neronov & Vovk, 2010; Alves Batista & Saveliev, 2021). Even such tiny magnetic fields are so volume filling, that all numerical modelling exclude that purely astrophysical magnetic seeding scenarios (see below) can reproduce the high filling factors required by blazar data (Bondarenko et al., 2022; Tjemsland et al., 2024).

Observational constraints on the magnetisation of the Universe before the formation of cosmic structures can be derived from the anisotropy of the CMB. Primordial magnetic fields affect the CMB through two principal mechanisms. First, through gravitational effects, they generate additional cosmological perturbations (scalar, vector, and tensor) that leave imprints on the angular power spectra. Second, magnetic fields dissipate during recombination and reionization. This dissipation transfers energy to the plasma, altering the thermal and ionization history of the Universe, which further modifies the CMB anisotropies and thermal spectrum (Paoletti et al., 2019). The observed absence of these distortions in the CMB anisotropy angular power spectra from Planck (Aghanim et al., 2020a) data allows setting upper limits on the strength of these primordial fields, typically on the order of a few comoving $\sim$ nG on $\sim$ Mpc scales (e.g. Paoletti et al., 2019; Planck Collaboration et al., 2016).

Mini-review of astrophysical seeding models - more in the context of simulations and models

Unlike primordial scenarios, astrophysical seeding models assume an initially unmagnetised Universe, in which magnetic fields are generated with formation of the first stars and galaxies. One promising mechanism for the creation of astrophysical magnetic fields is the Biermann battery, that arises in an ionized plasma when isodensity surfaces do not coincide with isobaric surfaces, and a current can be created via the baroclinic effect. This situation leads to the generation of magnetic fields at a rate (Ryu et al., 2011)

$$\frac{d\mathbf{B}}{dt} \sim \frac{m_e c}{e} \frac{\nabla \rho_e \times \nabla p_e}{\rho_2^2} \,. \tag{1.20}$$

This process operates during the formation of proto-galaxies as well as in compact objects such as accretion disks and stars. While the seed fields generated by this mechanism are extremely weak (typically $B \sim 10^{-20}$ G, Ryu et al. 2011), they can be rapidly amplified within collapsed objects. Since the dynamical timescales in accretion disks and stars are

relatively short, these tiny seeds can be rapidly amplified via dynamo action (Widrow et al., 2011). Once generated and amplified within galaxies, this magnetised plasma must be transported into the proto-galactic medium and the larger IGM to act as a cosmic seed. This expulsion is driven by galactic winds and AGN (e.g. Furlanetto & Loeb, 2001; Bertone et al., 2006). In particular, considering lower mass halos, the process is dominated by stars outflows, that through stellar winds and supernovae explosions are able to eject the magnetic fields along with mass into interstellar medium (ISM), circumgalactic medium (CGM) and into voids. At the high mass end, a more energetic mechanism is naturally provided by AGN. The SMBHs launch relativistic jets that can inflate immense radio lobes of highly magnetised plasma, that may eventually extend well beyond the boundaries of the host galaxy, penetrating deep into the surrounding environment. This process can efficiently magnetise the central volume of the clusters and even the IGM during their quasar phase (e.g. Donnert et al., 2018, and references therein).

Considering the properties discussed previously, such as their size and energy output (see 1.1 and 1.3), and given their ability to transport magnetic flux over Megaparsec scales, radio galaxies represent the most important candidate among all astrophysical seeding mechanisms.

One of the main goals of this Thesis is to investigate whether the largest observed GRGs are actually capable of injecting magnetised plasma into cosmic filaments and voids, or else if these extreme jets can also be interpreted in a different way, for example as the result of the γ-ray beam model proposed for Porphyrion, as we discussed in 1.3.3.

My Thesis work is aimed to investigate, for the first time, this scenario in a statistical way and using state-of-the-art cosmological simulation, and to assess which fraction of observed GRGs might be ascribed to this mechanism and would therefore not contribute to the astrophysical magnetisation of large-scale structures.

2

Methods

2.1 Cosmological Enzo simulation

In this work I used simulations made with the Enzo code, an adaptive mesh refinement (AMR), grid-based hybrid code (hydro + N-Body) which is designed to do simulations of cosmological structure formation. In particular, I analysed a recent cosmological simulation produced using the Enzo code (enzo-project.org), presented in Vazza et al. (2025) and designed to investigate the injection and evolution of cosmic rays and magnetic fields by different mechanisms operating in the cosmic web. The physical model used here yields the best comparison with recent LOFAR observations of the RRM as a function of redshift, RRM(z), as in Carretti et al. (2024) and Carretti & Vazza (2025). The simulated volume covers 42.5^3 Mpc^3 (comoving) with a static grid of 1024^3 cells, giving a constant spatial resolution of 41.5 kpc/cell and a constant mass resolution of 1.01×10^7 M$_\odot$ per dark matter particle. The run includes equilibrium gas cooling, a "sub-grid" dynamo amplification model at run-time, which allows the estimation of the maximum contribution of a dynamo in low density environments (see e.g. Vazza et al., 2017), while the treatment of primordial magnetic fields and feedback from galaxy formation processes was tailored to reproduce several key observables of the galaxy distribution (see Vazza et al. 2025 for further details).

The adopted star formation recipe follows the method by Kravtsov (2003), designed to reproduce the observed Kennicutt's law (Kennicutt, 1998) and with free parameters calibrated to reasonably reproduce the integrated star formation history and the stellar mass function of galaxies at $z \leq 2$. The feedback from star forming particles assumes a fixed fraction of energy/momentum/mass ejected per each formed star particles, $E_{SN} = \epsilon_{SF} m_* c^2$, with efficiency calibrated to $\epsilon_{SF} = 10^{-8}$ as in previous work (Vazza et al., 2017). The model also considers that 90% of the feedback energy is released in the thermal form (i.e. hot supernovae-driven winds), distributed among the 27 nearest cells around the star particle, and 10% in the form of magnetic energy, assigned to magnetic dipoles by each feedback burst. The feedback from AGN is implemented by allowing, at each time step of the simulation, the highest density peaks in the volume to evolve as they harbor a SMBH, to which we assign a realistic mass based on observed scaling relation (e.g. Gaspari et al., 2019). The code computes the instantaneous mass

growth rate onto each supermassive black hole by following the standard Bondi–Hoyle formalism, in which there is (as typically for simulations at this resolution) an ad-hoc "boost" parameter meant to compensate for the lack of resolution around the Bondi radius. Both "cold gas accretion" feedback (in which most of the energy is distributed in the form of thermal energy in the neighborhood of each simulated AGN) or "hot gas accretion" feedback (in which most of the energy is released in the form of bipolar kinetic jets) are used, depending on the temperature of the gas falling into each SMBH. In both cases, the feedback routine releases 10% of the feedback energy in the form of magnetic energy, through pairs of magnetised loops wrapped around the direction of kinetic jets. This magnetic field is added to the simulation, leading to "magnetic bubbles" correlated with halos in the simulated volume. A more detailed description of all parameters used in this and in the other model variations of the entire suite of cosmological simulations is given in Vazza et al. (2025).

The extragalactic magnetic field model

Of chief importance for our study is the assumed magnetic field in the volume. The magnetisation level in the chosen run is predominantly primordial, but also a realistic level of additional magnetic "pollution" by galaxies is considered.

The stochastic primordial initialization of the magnetic field is obtained by drawing magnetic field vectors from a power-law spectrum: $P_B(k)dk = P_{B0}k^{-1}dk$, and with a normalization set to $(\langle B^2 \rangle)^{0.5} \approx 0.37\,\mathrm{nG}$ after smoothing the field to a physical scale of 1 Mpc (comoving), as usually done in CMB analysis (e.g. Paoletti & Finelli, 2019). Such magnetic field normalization is ~ 5 times below the existing constraints from the best analysis of CMB, and is driven by recent analysis of the distribution of RRM in LOFAR radio observations by (e.g. Carretti & Vazza, 2025).

Carretti & Vazza (2025) argued that this primordial magnetic model, complemented with a realistic astrophysical contribution from the activity of galaxies, can well reproduce a number of real observations in the radio sky, recently reported using different telescopes and by different independent groups:

- the redshift distribution of observed RRM until $z \sim 3$ reported by Carretti et al. (2024);
- the detection of the synchrotron signal by relativistic electrons accelerated in filaments by structure formation shocks, obtained via stacking analysis of $\sim 10^5$ pairs of galaxies (Vernstrom et al., 2021, 2023).

- the recent inferred distribution of Faraday Rotation in the outskirts of nearby galaxy groups ($z \leq 0.1$) obtained by Anderson et al. (2024) using ASKAP.

Figure 2.1 shows the example of the observed trend of the Residual Rotation Measure of polarized background sources located at different redshifts recently measured with LOFAR, and the comparison with the predictions from a few models for extragalactic magnetic fields realised with ENZO. The model chosen for this Thesis is the C1 model in the Figure, which comprises a combination of primordial and astrophysical sources of magnetic fields. The other two models shown here only contain variations of astrophysical seeding scenarios of magnetic fields, and are unable to match the observed trend of $RRM(z)$ from sources at high redshift.

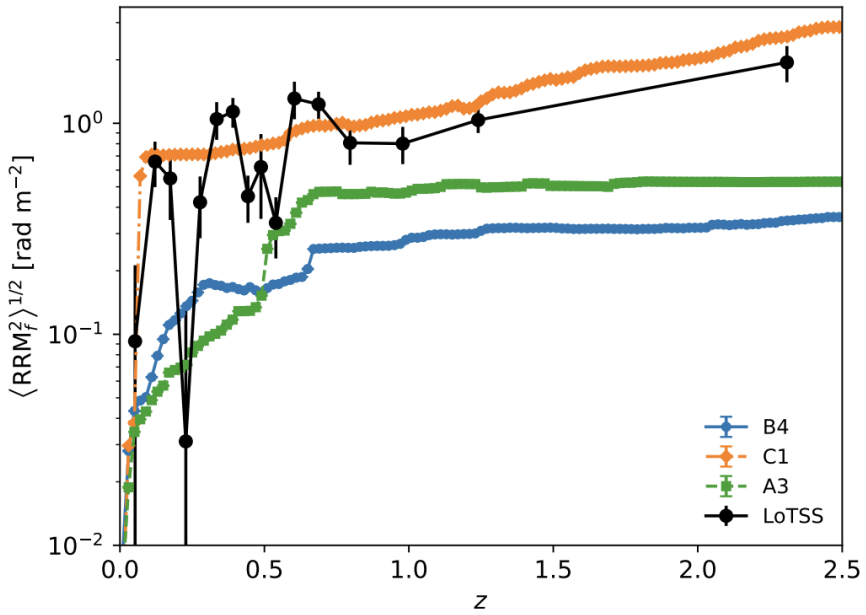

Figure 2.1. Observed trend of the Residual Rotation Measure of polarized background sources located at different redshifts (black points with error bars) measured using LOFAR by Carretti et al. (2024), and comparison with a few model realization of cosmological MHD simulations (lines with colors). The model chosen for this Thesis is the C1 model, which comprises a combination of primordial and astrophysical sources of magnetic fields. The other two models shown here only contain variations of astrophysical seeding scenarios of magnetic fields, and are unable to match the observed trend of $RRM(z)$ from sources at high redshift (see Vazza et al. 2025 for more details).

For this work I used 5 snapshots at different redshift (z), listed in Table 2.1

Table 2.1. Simulation snapshots used in the analysis and their corresponding redshift.

Snapshot ID	Redshift
19	1.065
21	0.835
22	0.675
24	0.312
26	0.100

Each snapshot contains the baryon and dark matter density fields, gas temperature, and magnetic field vector components. Since the simulation evolves these quantities in a comoving reference frame, a crucial distinction must be made between comoving and physical units: while the former are convenient for cosmological evolution, radiative processes, such as synchrotron radiation or inverse Compton scattering, depend on the physical state of the plasma at a specific epoch. Consequently, the code's output must be converted by accounting for the cosmic scale factor, $a = (1+z)^{-1}$. In general, a physical quantity $Q_{\rm phys}$ is related to its comoving counterpart $Q_{\rm com}$ by a factor $(1+z)^n$, where n depends on the dimensionality of the quantity (e.g., $n = 3$ for density, as physical volume scales as $V_{\rm phys} \propto (1+z)^{-3}$). While the gas temperature is provided directly in Kelvin, the density and magnetic field values are stored in internal code units. We convert these to physical CGS units using the density factor $\rho_0 = 2.82 \times 10^{-30}\,\mathrm{g\ cm^{-3}}$, the velocity factor $v_0 = 1.258 \times 10^9\,\mathrm{cm\ s^{-1}}$ and the redshift of the snapshot z, according to the following relations (2.1):

$$\begin{aligned} \text{Density (Physical):} \quad & \mathcal{C}_{\rho,\rm phys} = \rho_0\,(1+z)^3, \\ \text{Density (Comoving):} \quad & \mathcal{C}_{\rho,\rm com} = \rho_0\,, \\ \\ \text{B-Field (Physical):} \quad & \mathcal{C}_{B,\rm phys} = \sqrt{4\pi\rho_0}\,v_0\,(1+z)^2, \\ \text{B-Field (Comoving):} \quad & \mathcal{C}_{B,\rm com} = \sqrt{4\pi\rho_0}\,v_0\,. \end{aligned} \tag{2.1}$$

The cosmological volume can be visualized through a set of 2D maps with a resolution of 1024×1024 pixels. These maps are generated by computing the mean value along the line of sight (LOS) for each pixel of the grid. Figure 2.2 shows the projected distributions of baryonic density, dark matter density, and magnetic field intensity $|B| = \sqrt{(B_x^2 + B_y^2 + B_z^2)}$ for redshift $z = 1.065$, $z = 0.675$ and $z = 0.1$. These maps

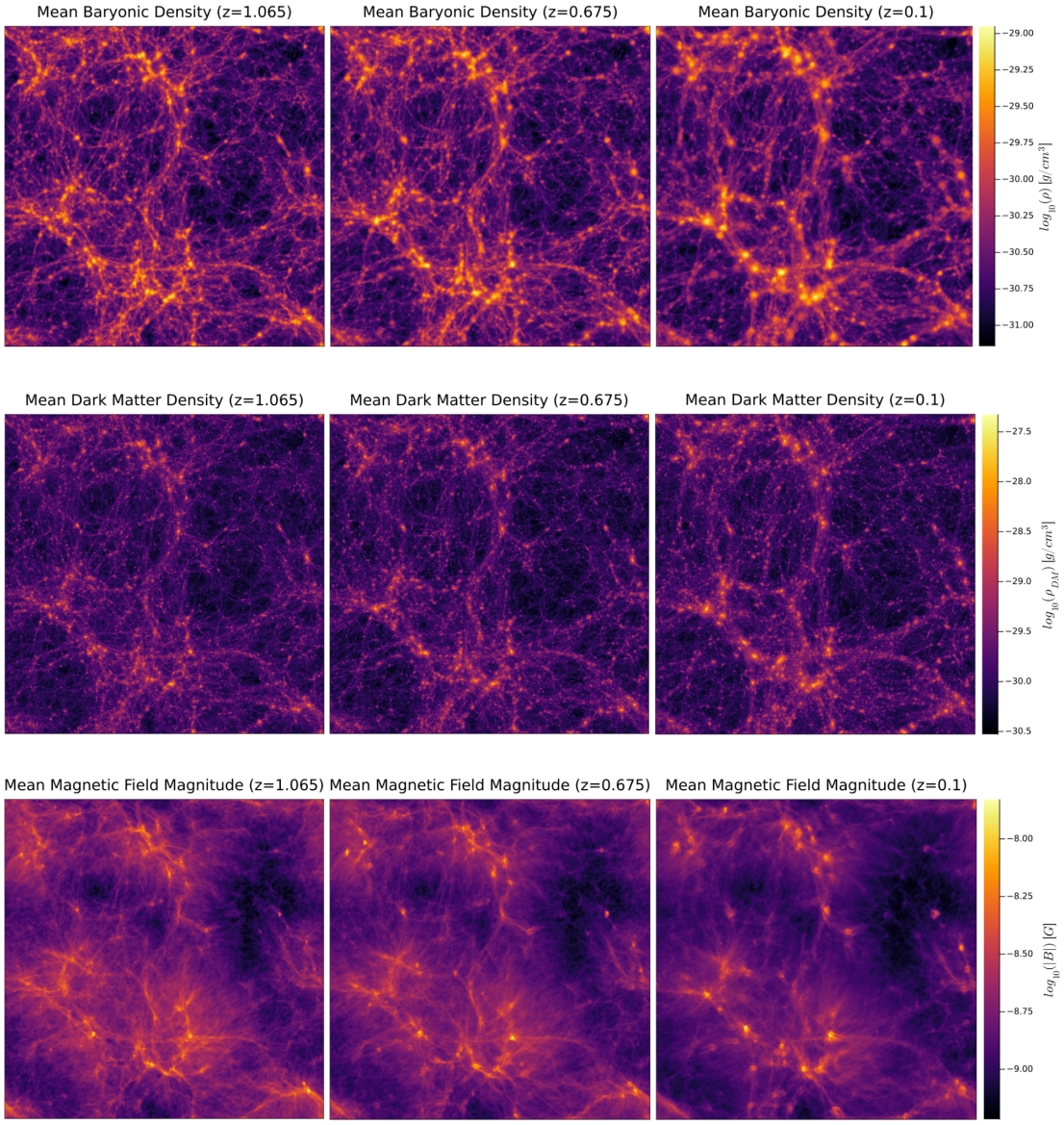

Figure 2.2. Two-dimensional maps of projected volume-weighted mean baryon density (top panels, in units of comoving g/cm^3), dark matter density (central panels, same units) and magnetic field intensity (bottom panels, in units of comoving Gauss) across the full $(42.5\,\mathrm{Mpc})^3$ simulated volume for the $z = 1.065$ (left), $z = 0.675$ (centre) and $z = 0.100$ (right) epochs.

highlight the significant structural evolution of the volume. As redshift decreases, the large-scale structure becomes increasingly pronounced, with matter flowing from voids into filaments and collapsing into high-density knots. Moreover, significant amplification

of the magnetic field magnitude within clusters and filaments can be observed. This magnetisation of high-density regions is driven by two main physical processes. The first one is the small-scale dynamo, that amplifies magnetic fields through turbulence induced by structure formation. However, as in all finite volume simulations the efficiency is here limited by numerical resolution: to completely resolve the dynamo amplification, a large Reynolds number ($R_e \gg 1000$) is required, but numerically this scales as $\mathrm{Re} \sim R_{\mathrm{vir}}/\Delta x$ (where Δx is the resolution element), making it a challenge task for simulations which can, at best, resolve the internal structure of massive halos with 100^3 resolution elements or less (Donnert et al., 2018). The second process, more significant in our case, is the injection of magnetic fields by astrophysical feedback mechanisms within halos: this simulation includes sub-grid parameters for magnetic seeding driven by star formation and AGN jets, which contribute to the high field values observed in the collapsed structures, as detailed in Vazza et al. (2025). This ensures that the 3-dimensional model of magnetic fields in the simulation is, at present, the most realistic which can be found in cosmological numerical simulations.

The simulation also provides for each snapshot a catalog of halos with important properties, including their 3-dimensional location, their virial radius R_{200}, their total virial mass M_{200}, their baryonic virial mass M_{200Bar} and their virial Temperature T.

2.2 New numerical routines produced for this Thesis

This section is devoted to the description of the numerical tools and analysis routines which I developed specifically for this work, using the Julia programming language. The primary objective of the code is the post-processing of simulation data to identify and characterize "Porphyrion-like" objects and to study their properties statistically.

Specifically, I will outline the physical criteria adopted for halo selection, which is necessary to isolate suitable candidates for the study. Subsequently, I will discuss the technical implementation of the routines, concerning the creation of jets from SMBHs, with particular attention to the handling of the periodic boundary conditions of the cosmological volume. Finally, I will detail the procedures used to derive the observable statistics of the simulated population, specifically focusing on the computation of their projected length distributions and the modelling of their expected radio and γ-ray luminosities.

2.2.1 Halo selection criteria

To identify the structures within the volume that are suitable for our study, we require objects at least as massive as the halo hosting Porphyrion: $M_{Porp} \sim 10^{12} M_{\odot}$. Using the information provided from the halo catalogs produced by the analysis of the simulation, which are based on a classical spherical overdensity reconstruction of halos, and were already generated in previous work (Vazza et al., 2025), I can construct the differential and the cumulative mass distribution of halos, highlighting the mass selection criteria. This is showed in Figure 2.3 for redshift $z = 1.065$ and $z = 0.1$.

The number of suitable halos with $M_{200} \geq 10^{12} M_{\odot}$ is listed in Table 2.2, and can be visualized in the 3D map in Figure 2.4, where the baryonic density field of the simulation is mapped for $z = 1.065$ and $z = 0.1$, downsampled by a factor of 16 for visualization purposes. All further analysis will be done on these selected halos.

Table 2.2. Redshift, total number of halos, and number of selected halos for each simulation snapshot.

Snapshot ID	Redshift	Total Halos	Selected Halos
19	1.065	1758	70
21	0.835	2020	95
22	0.675	2180	108
24	0.312	2619	148
26	0.100	2866	163

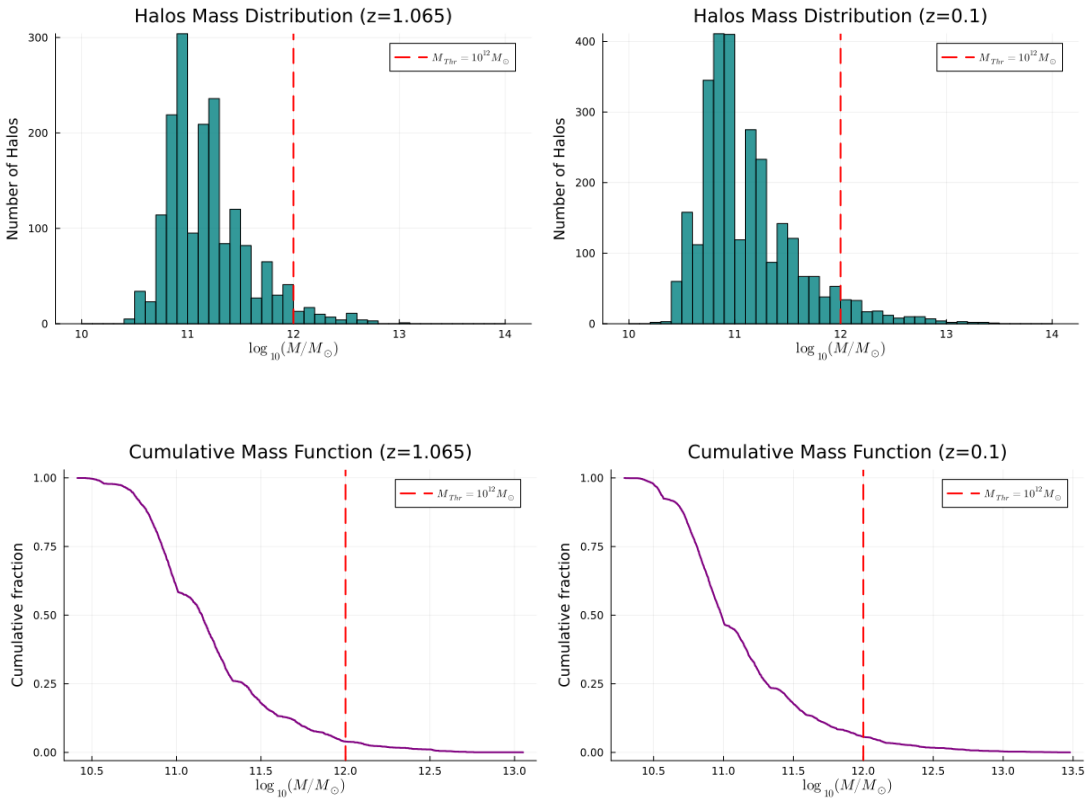

Figure 2.3. Differential halos mass distribution (top panels) and cumulative mass function (bottom panels) for $z = 1.065$ (left) and $z = 0.1$ (right) epochs. The red dashed line highlights the mass selection limit.

2.2.2 Modelling the trajectories of γ-ray beams from active galactic nuclei

The goal of this analysis is to build a sample of Porphyrion-like objects within our cosmological volume. Consequently, the first step is to simulate the propagation axes of bipolar jets originating from the SMBHs hosted within the selected halos. These beams are extended on both sides to reach the observed length of Porphyrion. This will allow me to investigate their characteristics, such as the physical properties of the surrounding medium and, in particular, the magnetic field through which the jets propagate. This approach leads to an overestimation of the jet population; however, the introduction of a duty cycle would, in principle, only affect the frequency of observable jets rather than their statistical distribution. For this reason, I do not need to pre-select a specific fraction of active jets; instead, I consider all selected candidates as active.

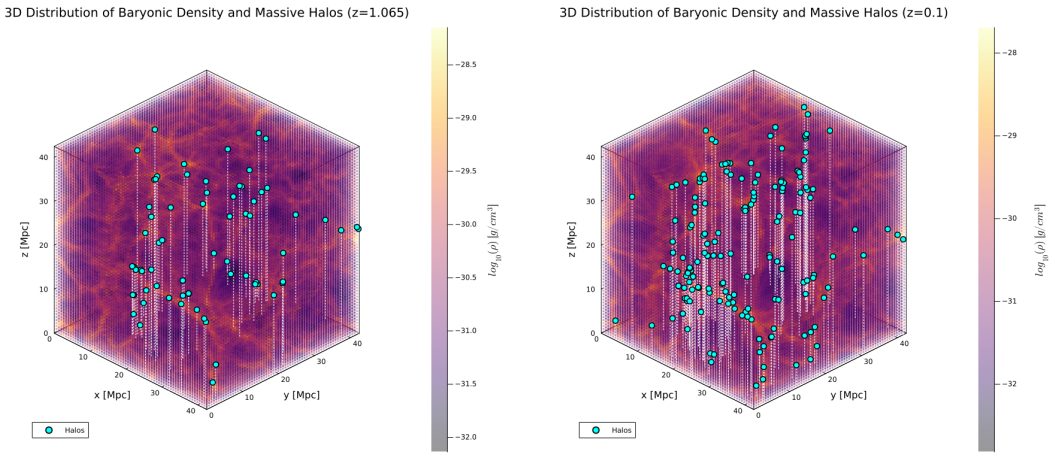

Figure 2.4. 3D visualization of baryonic density (in units of comoving g/cm^3) within the full simulation volume ($V_{\rm sim} = 42.5^3\,{\rm Mpc}^3$) at $z = 1.065$ (left) and $z = 0.1$ (right), rendered with a downsampling factor of 16. Cyan circles indicate the positions of halos with mass $M_{200} > 10^{12} M_\odot$. Vertical dashed lines connect each halo to the xy plane ($z = 0$) to facilitate spatial depth perception.

Operatively, in my analysis I have assumed that the centre of each selected halo in the catalog host a SMBH, and thus I model jets as a straight line passing through the halo centre. To define the jet orientation in 3D space, I randomly extract two angles, θ and ϕ, such that:

$$\theta = \pi \cdot \mathcal{R}_1$$

$$\phi = 2\pi \cdot \mathcal{R}_2$$

where $\mathcal{R}_{1,2}$ are random numbers uniformly distributed in the interval $[0, 1]$. These angles allow me to define a unit direction vector $\mathbf{u}$:

$$\mathbf{u} = [\sin\theta\cos\phi,\ \sin\theta\sin\phi,\ \cos\theta]. \tag{2.2}$$

Consequently, the jet is represented as a segment passing through the halo centre aligned with $\mathbf{u}$. The total length of the structure is fixed to $L_{\rm jet} = 13.272$ Mpc (comoving), matching the estimated comoving extent of the Porphyrion system at its discovery redshift ($L_{\rm Com} = L_{\rm Phys}\cdot(1+z_{\rm Porph}) = 7\cdot(1+0.896) = 13.272$). At this stage, it is possible to extract the physical properties of the medium, specifically density, temperature, and magnetic field magnitude ($|B|$), at each point along the line. To summarize, this procedure generates a one dimensional profile of the traversed environment along a randomized direction. An example is showed in Figure 2.5 for a generic halo at $z = 1.065$.

To provide a baseline for comparison with the physical properties sampled along the jet trajectories, I also computed the spherically averaged radial profiles. To do so, I calculated the distance of every grid cell from the halo centre and allocated the physical quantities into concentric spherical shells. The width of each shell was set to match the simulation grid resolution ($\Delta x = 0.041$ Mpc comoving). I used a volume-weighted approach: since the simulation uses a uniform grid, all cells possess identical volumes, hence the profile value in each shell is computed as the simple arithmetic mean of all cells in that radial bin. It should be noted that, in the baseline framework, the same length L_{jet} and orientation $\mathbf{u}$ are applied to all simulated jets, independently of the selected halo. To increase statistics, the generation and analysis of jet properties is iterated a large number of N random extractions of jet directions for the same set of halos, which ensures the construction of a statistically significant sample.

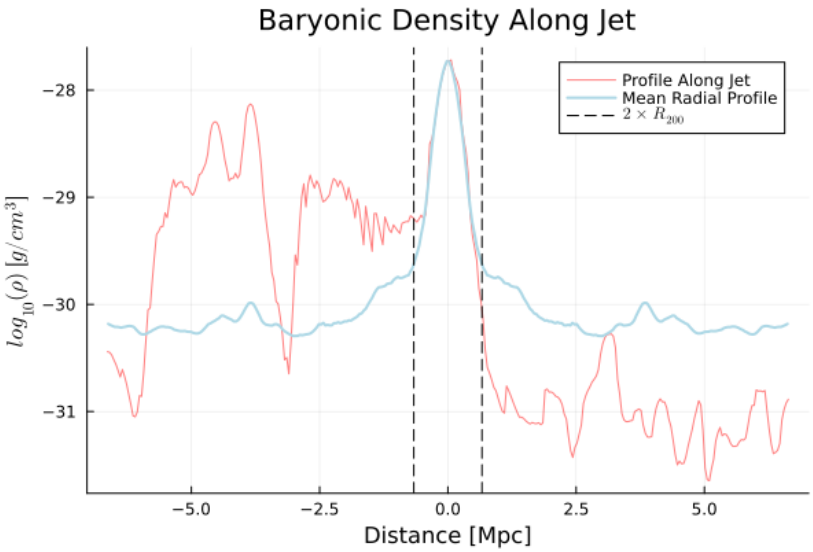

Figure 2.5. Physical properties along jet trajectories *(Continued on the next page).*

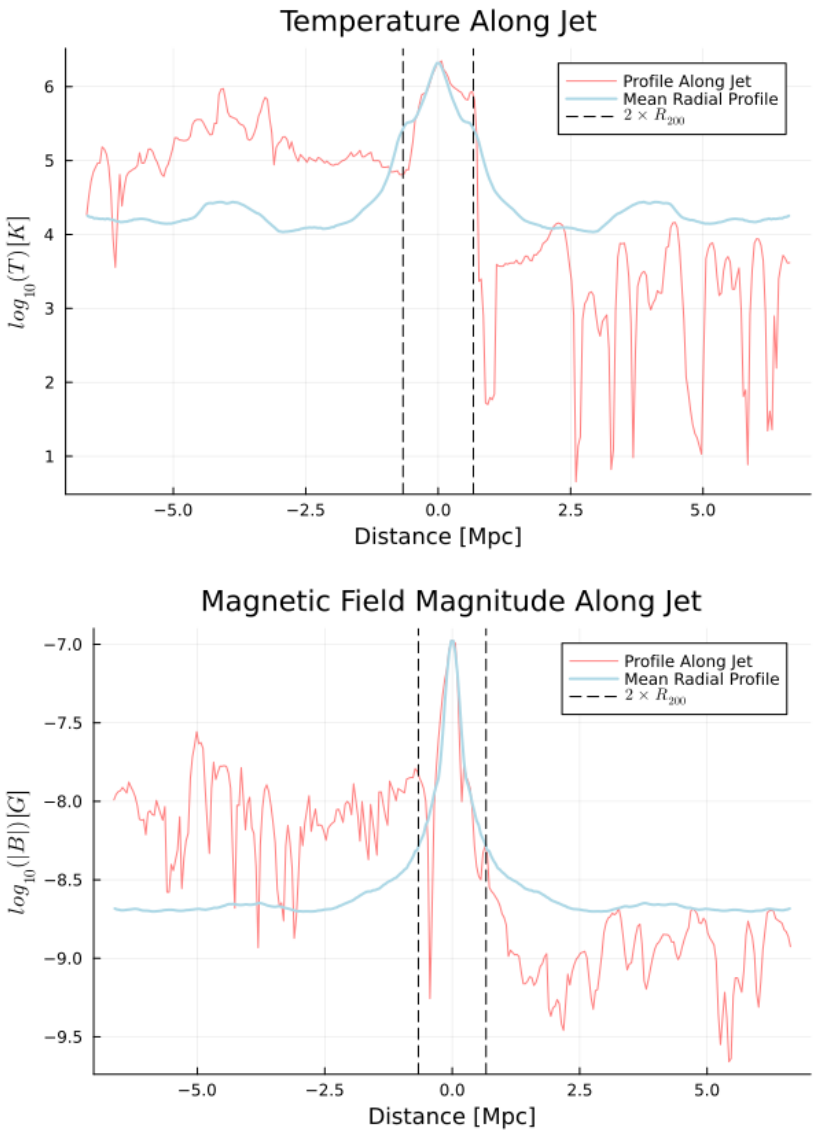

Figure 2.5. *(Continued from previous page).* Profiles of the baryonic density (top panel, in units of comoving g/cm^3), gas temperature (middle panel, in K) and magnetic field intensity (bottom panel, in units of comoving Gauss) extracted along a simulated jet trajectory of $L_{\rm jet} = 13.272$ comoving Mpc, for a generic halo at $z = 1.065$. The x-axis represents the distance (in comoving Mpc) along the jet axis relative to the halo centre (located at 0); positive and negative values correspond to the two opposite directions of the bipolar flow. The red line (Profile Along Jet) shows the local values sampled along the specific jet path. The light blue line (Mean Radial Profile) represents the spherically averaged, volume-weighted radial profile of the environment. Vertical dashed lines mark the boundary at $2 \times R_{200}$.

2.2.3 Modelling of periodic boundary conditions

Given the considerable length of the simulated jets ($L_{\rm jet}$ = 13.272 Mpc), which is comparable to a significant fraction of the simulation box size, there is a high probability that a jet extends beyond the boundaries of the computational domain. To handle this issue, a straightforward solution is to apply periodic boundary conditions (PBC), considering that the ENZO simulation indeed treated this volume as fully periodic. The PBC is implemented by forcing the particles near a boundary to interact with the ones near the opposite boundary. To satisfy conservation of mass within the region of interest, the particles exiting the domain are forced to enter the opposite inflow boundary while keeping the same physical properties. I applied the same principle to the jet geometry: whenever the coordinates of a sampling point along the jet satisfy $x_i < 1$ or $x_i > N_{\rm grid}$ (where $N_{\rm grid} = 1024$ is the grid resolution), they are wrapped around the box to ensure continuity in the sampling of physical fields. In Figure 2.6 there is a schematic representation of the implementation of PBC, in which the host dark matter halo is located on the right side of the simulation box and the jet segment exiting the right boundary is wrapped around to the opposite (left) side. This approach guarantees that no numerical artifacts are introduced at the edges and that the statistical properties of the jets are preserved regardless of their position relative to the box boundaries. For completeness of information, the mean radial profiles were computed within the simulation box limits, as applying periodicity to the spherical averaging does not provide a significant advantage for the results we want to achieve.

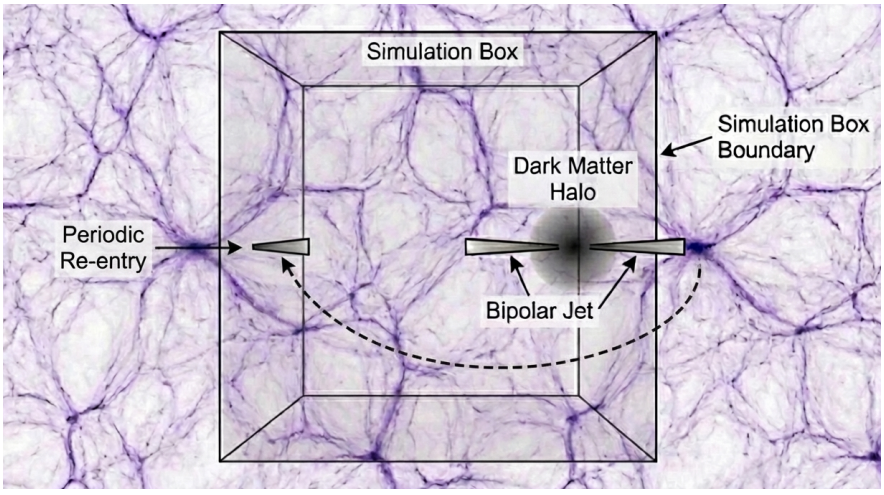

Figure 2.6. The diagram illustrates a schematic view of how periodic boundary conditions are implemented. The host dark matter halo is placed close to the simulation box margins. The jet exiting the right boundary re-enters from the left boundary.

2.2.4 Definition and calculation of observable jet lengths

To determine the potential observability of the simulated jets, I closely modelled the physical scenario proposed for the Porphyrion system by Neronov et al. (2025). In this model, the observed radio emission is interpreted as synchrotron radiation produced by secondary electron-positron pairs deposited into the intergalactic medium by a very high-energy gamma-ray beam emitted by the AGN. A critical condition for this emission to be detectable is the interaction of these pairs with a sufficiently strong magnetic field. Following the constraints derived from the non-detection of inverse Compton emission in the Porphyrion system, I established a reference lower bound for the comoving magnetic field strength of $B_{\rm ref} = 8$ nG. Regions of the jet traversing environments with $B < B_{\rm ref}$ would likely remain radio-dark or below current detection limits. To estimate the sensitivity of my results to this parameter, I used the comoving magnetic field strength of cells in the simulation at a given redshift, and I chose three distinct comoving magnetic field thresholds:

- **Fiducial Threshold:** $B_{\rm thr} = 8$ nG (corresponding to a proper magnetic field of $B = B_{\rm thr}(1+z)^2 \simeq 30\,{\rm nG}$ at the redshift of the source), based on the Porphyrion lower bound;
- **Low Threshold:** $B_{\rm thr} = 4$ nG (corresponding to a proper magnetic field of $B \simeq 15\,{\rm nG}$), probing more extended, fainter structures;
- **High Threshold:** $B_{\rm thr} = 16$ nG (corresponding to a proper magnetic field of $B \simeq 60\,{\rm nG}$), probing only the most magnetised peaks, typical of filament cores.

I implemented a numerical routine to process the radial profiles of the simulated jets. For the selected sample of halos, I analyse the magnetic field distribution along the propagation axis. The primary goal is to determine the statistical probability that a galaxy hosting a gamma-ray beam of a comoving length $L_{\rm Com} = 13.272$ produces an observable radio structure comparable to Porphyrion. Since the magnetic field along the jet path is not uniform but fluctuates due to the interaction with the cosmic web (e.g., crossing voids vs. filaments), the "observable length" is not a trivial geometric parameter. I therefore introduced two metrics to define the size of the emitting structure:

1. **Effective Length ($L_{\rm eff}$):** defined as the summation of the simulation cells where the magnetic field exceeds the chosen threshold ($B > B_{\rm thr}$). This metric represents the length capable of producing significant synchrotron emission.
2. **Maximum Length ($L_{\rm max}$):** defined as the spatial distance between the first and the last cells along the jet axis satisfying the condition $B > B_{\rm thr}$. This definition

is less restrictive than L_{eff}, as it includes regions of low magnetic field that may exist between bright knots.

The routine allows me to filter the simulated population based on these metrics, selecting candidates that exceed a specific length or identifying systems that reach a defined percentage of Porphyrion's size under different magnetic field assumptions.
In addition to the intrinsic length, we must consider that real astronomical observations only reveal the projected size of a structure on the plane of the sky. This is due to geometric projection effects: a three-dimensional structure is observed as a two-dimensional image projected onto the plane of the sky. To compare my simulated intrinsic jet length with hypothetical observations, I have taken into account the random orientation of the jets with respect to an observer. Essentially, I assign a random viewing angle to each direction of the jet by extracting $\mu = \cos(\theta)$ from a uniform distribution $\mathcal{U}[0, 1]$. Following Oei et al. (2023), the corresponding projected length L_{proj} is then derived from the intrinsic length L_{Int} as:

$$L_{\text{proj}} = L_{\text{Int}} \sin(\theta) = L_{\text{Int}} \sqrt{1 - \mu^2}. \tag{2.3}$$

By applying this transformation, I generate a statistical distribution of observable lengths that accounts for the shortening effect arising from the projection.

2.2.5 Generation of the observable statistics of γ-ray beams

To characterize the simulated jet population in this model in a statistical way, in this Thesis I computed the distribution functions of the intrinsic and of the projected length of jets, as a function of the key model parameters. For each simulated jet, I evaluated the maximum length satisfying a specific comoving magnetic field threshold ($B_{\text{thr}} \in \{4, 8, 16\}$ nG). Furthermore, to allow a direct comparison with real astronomical observations, I included the effect of projection along the line of sight for random viewing angles. Using these projected lengths, I constructed two kinds of cumulative distributions:

- **Normalized Cumulative Distribution:** I pooled together the jet lengths from all five redshift snapshots (from $z = 0.1$ to $z = 1.065$). I normalized the resulting cumulative by the comoving volume of the simulation box ($V_{\text{sim}} = 42.5^3\,\text{Mpc}^3$) and then divided by the number of times the volume was simulated (N extractions $\cdot\, 5$, the number of simulation snapshots used). This distribution evaluates the number density of the structures produced.

- **Volume-Weighted Cumulative Distribution:** To estimate the total number of expected sources in the entire sky, the simulation counts have to be scaled to the actual cosmological volume I aimed to simulate. To do so, I first divided the observable Universe volume into five continuous spherical shells based on our snapshot redshift z. I defined the boundaries of these shells as follows: the first shell spans from $z = 0.0$ to $z = 0.1$, the second from $z = 0.1$ to $z = 0.312$, and so on, up to the fifth outermost shell covering the interval from $z = 0.835$ to $z = 1.065$. I then derived the weight factor for each snapshot by computing the ratio between the comoving volume (Equation 2.5) of the respective spherical shell and the volume of the simulation box, adjusted for the times the volume was simulated (N extraction). The shell volumes and the corresponding ratio for each redshift interval are reported in Table 2.3. This approach assumes that the physical and statistical properties derived from a specific snapshot (e.g. $z = 1.065$) are representative of the entire redshift interval of its corresponding shell and yields a realistic prediction of the all-sky source counts.

To evaluate the comoving volumes, I adopted the same flat ΛCDM cosmology of the cosmological simulation, i.e. a set of parameters consistent with the Planck Satellite results (Aghanim et al., 2020b): $H_0 = 67.8\,\mathrm{km\,s^{-1}\,Mpc^{-1}}$, $\Omega_m = 0.308$, and $\Omega_\Lambda = 0.692$. In this framework, the line of sight comoving distance D_C at redshift z is defined by (Hogg, 2000):

$$D_C(z) = \frac{c}{H_0} \int_0^z \frac{dz'}{\sqrt{\Omega_m (1+z')^3 + \Omega_\Lambda}}\,, \tag{2.4}$$

where c is the speed of light. Consequently, the comoving volume V_C enclosed within a sphere of radius D_C is calculated as:

$$V_C = \frac{4\pi}{3} D_C^3\,. \tag{2.5}$$

As introduced in Section 2.2.2, my approach assumes a continuous jet propagation for all selected halos at all times, without including any realistic duty cycle of AGNs. For this reason, the obtained distributions are an absolute upper limit. To account for the AGN duty cycle and to contrast the predicted distributions of jets with real data, I compared the simulated curves with the projected lengths of observed GRGs. In particular, I reproduced the data from Andernach & Brüggen (2025) showed in Figure 2.7, with a close focus on GRGs larger than 3 Mpc. To ensure a consistent comparison with the observational catalog, which is approximately limited to $z \sim 1$, the simulated counts were rescaled by the ratio between the comoving volume enclosed within $z = 1$ and the total volume sampled by the simulation (yielding a factor $f \sim 0.87$,

Table 2.3. The comoving shell volumes and the weight factors for the five redshift range analysed in my Thesis.

Redshift Range	**Shell Volume** [Gpc^3]	**Weight factor** $V_{\rm shell}/V_{\rm sim}$
$[0.835, 1.065]$	78.93	1.03×10^6
$[0.675, 0.835]$	43.37	5.65×10^5
$[0.312, 0.675]$	56.94	7.42×10^5
$[0.1, 0.312]$	8.37	1.09×10^5
$[0.0, 0.1]$	0.34	4.39×10^3

which is close to unity given that $z_{\rm sim,max} = 1.065$). Subsequently, I evaluated the ratio between the observed and simulated cumulative counts at a reference length of 3 Mpc. This comparison yielded a scaling factor that was used to reduce the simulated counts to match the observed population. From a physical perspective, this normalization factor can roughly be interpreted as the introduction of an effective duty cycle for the population of AGN capable of driving TeV γ-ray emission and produce radio emission up to the level observed in Giant Radio Galaxies. This normalization allowed me to build a realistic simulated distribution of active sources, from which further radiative properties could be predicted.

2.2.6 Simulated maps of radio and γ-ray emission

In order to visually and physically characterize the environment crossed by the simulated jets, I developed a two-dimensional mapping procedure. It is worth stressing that this 2D mapping is just an illustrative "toy model", in which the actual time-dependent propagation of photons and the energy evolution of electrons and positron pairs as a function of their distance from their source is not modelled at all. Computing the exact radiative maps across a full 3D grid for the entire simulated population is instead more complex and is deferred to future work. Therefore, while this 2D approach allows us to visualize the local radiative conditions for a generic example halo, on a cell by cell basis along the direction of the γ-ray beam, the quantitative all-sky distributions presented in the subsequent Section 2.2.7 will use instead a simplified approach, in which to compute the total radio emission of each object I assign to each entire γ-ray beam the root mean square magnetic field previously extracted along the entire jet length.

To construct the 2D maps here, I used the information from a 3D cube centred on a generic selected halo, with side length corresponding to the total length of the simulated jets (13.272 comoving Mpc). Then, I extracted 2D slices from the 3D grid,

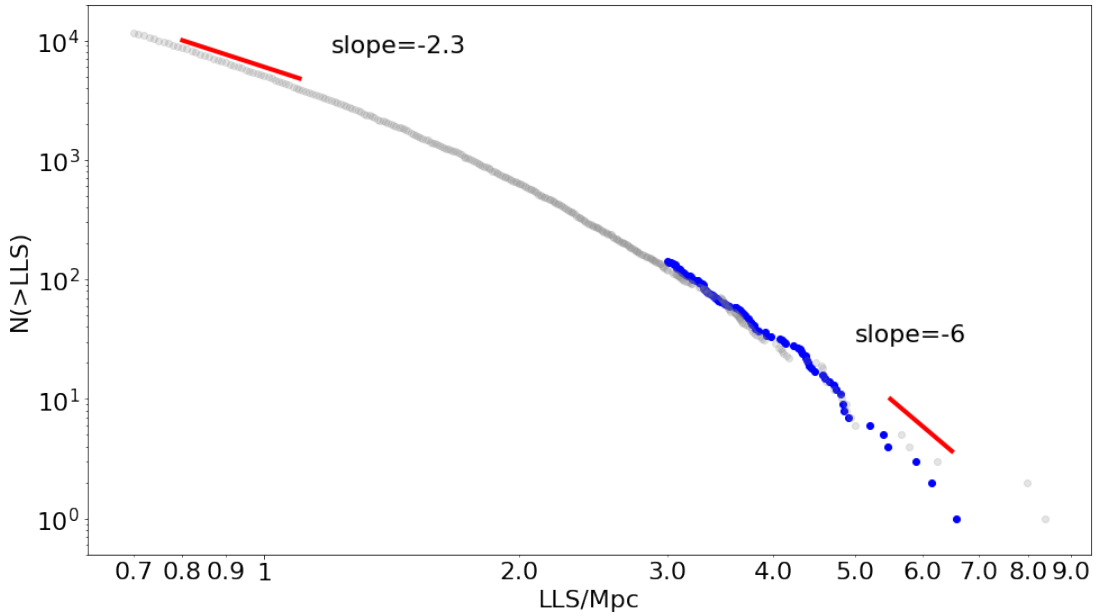

Figure 2.7. The number of known GRGs larger than a given largest linear size (LLS) as function of LLS. Blue dots are for 143 GRGs > 3 Mpc, and grey dots are from Mostert et al. (2024). The lines of fixed slope in this log-log plot are shown for reference. Image reproduced from Andernach & Brüggen (2025).

choosing the plane of extraction to be longitudinal to the jet axis. This choice allows for a direct visual investigation of the plasma environment that the jet encounters during its propagation. For visual purposes, the coordinates are rotated so that the jet path lies horizontal on the map. The first map generated using this approach represents the spatial distribution of the magnetic field magnitude. An example for a potentially detectable γ-ray beam is shown in Figure 2.8.

To link this simulated environment to actually observable quantities, I applied the γ-ray beam theoretical framework introduced in Section 1.3.3 (Neronov et al., 2025). The expected synchrotron emission frequency ($\nu_{\rm sync}$) generated by the 30 GeV electrons was calculated in the 2D environment. To do so, I used Equation (1.2), applying the appropriate B field for each pixel. To investigate and isolate the regions capable of sustaining high-frequency synchrotron emission, I also applied a masking technique to these frequency maps. I selected three proper magnetic field thresholds: $4 \cdot (1+z)$ nG, $8 \cdot (1+z)$ nG, and $16 \cdot (1+z)$ nG. The corresponding threshold frequencies were calculated with Equation (1.2), and the maps were masked by filtering out all cells where the local synchrotron frequency falls below the given threshold. An example of these "masked emission frequency maps" is shown in Figure 2.8.

Lastly, using the local proper magnetic field B in each cell, I also evaluated the expected inverse Compton to Synchrotron flux ratio ($F_{\rm IC}/F_{\rm syn}$) in each pixel, according to Equation (1.3). Specifically, the scaling used for this ratio is (Neronov et al., 2025):

$$\frac{F_{\rm IC}}{F_{\rm syn}} \simeq 10^6 \left[\frac{B}{10\,{\rm nG}}\right]^{-2}. \tag{2.6}$$

The resulting map in Figure 2.8 shows the ratio between high-energy and radio emission.

Overall, this example shows that indeed a γ-ray beam propagating along favorable lines of sight through the cosmic web can successfully generate collimated synchrotron emission at the appropriate radio frequencies and power levels. This 2D visualization shows how the model naturally accounts for the appearance of random bright "knots" along the jet axis, closely resembling the morphology observed in the Porphyrion system. These knot-like structures are a direct consequence of the random magnetic field fluctuations inherent to the IGM.

2.2.7 Modelling the full-sky distributions of radio and γ-ray emission from γ-ray beams

Once the calibrated volume-weighted distribution is available, it is possible to predict the observable radio and γ-ray fluxes of the simulated sources by adopting a set of physically motivated assumptions. The primary objective of this procedure is to compare our theoretical predictions with the sensitivity limits of modern surveys, yielding a quantitative estimate of the number of sources potentially detectable by LOFAR in the radio band and Fermi-LAT in the γ-ray spectral range, also considering that our model predicts that a fraction of this sources should already be in catalogs of radio galaxies. To accurately evaluate the radiative processes, all relevant physical quantities were converted from comoving to proper units.

As a first scaling assumption for the radio flux ($F_{\rm rad}$), it is assumed that the intrinsic synchrotron emission scales *linearly* with the physical length of the jets. Indeed it could be argued whether the power scales linearly with length (and therefore we assume that the jet thickness remains constant), or with the square of the length, assuming that the thickness also varies. Considering the jets as a beam of photons, we believe it is more realistic to assume that the linear scaling with the length is a more plausible choice here. Furthermore, the observations of Porphyrion were used as a calibrator, adopting a radio flux of $F_{\rm ref} = 10^{-16}\,{\rm erg\,cm^{-2}\,s^{-1}}$ (Neronov et al., 2025) at a reference length $L_{\rm ref} = 7\,{\rm Mpc}$ and redshift $z_{\rm ref} = 0.896$. I also accounted for the cosmological dimming effects on the flux due to the redshift of all sources in my catalog. In an expanding

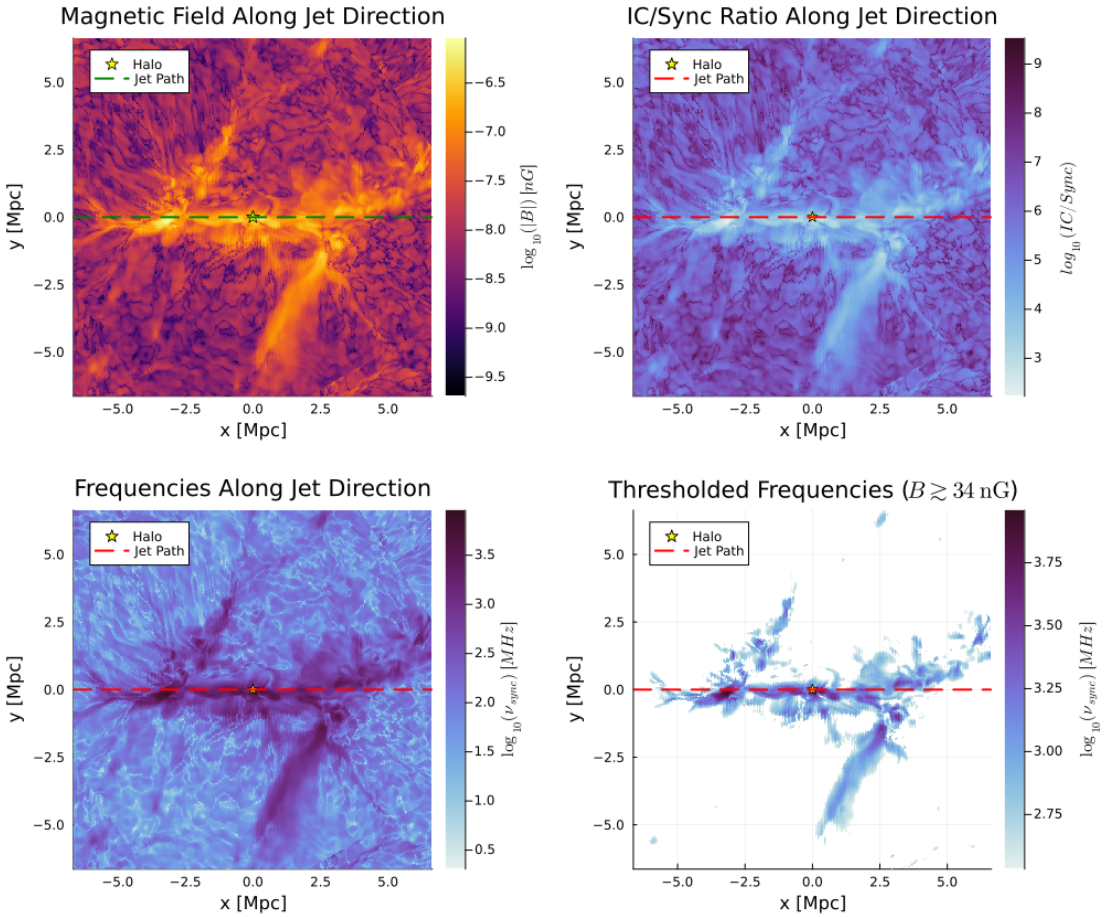

Figure 2.8. Two-dimensional longitudinal slices of the environment surrounding a simulated jet at $z = 1.065$ (the horizontal dashed line represents the jet axis, with the host halo at the origin). Top Left: Spatial distribution of the proper magnetic field magnitude. Top Right: Map of the expected inverse Compton to Synchrotron flux ratio ($F_{\rm IC}/F_{\rm syn}$). Bottom Left: Expected synchrotron emission frequency map, computed assuming a secondary electron energy of 30 GeV. Bottom Right: Thresholded synchrotron frequency map. Cells yielding an emission frequency below the limit associated with a local magnetic field of 34 nG have been masked. This isolates only the highly magnetised regions of the cosmic web where high-frequency radio emission would actually be observable. All color maps are in logarithmic scale.

Universe, the observed flux F of a source with intrinsic luminosity L scales with the square of its luminosity distance D_L according to the relation:

$$F = \frac{L}{(4\pi D_L^2)} \,. \tag{2.7}$$

In a flat ΛCDM cosmology, the luminosity distance scales with the redshift z as

$D_L(z) = (1+z)D_C(z)$, where D_C is the line of sight comoving distance (Equation 2.4). In addition to this geometric dimming, an extra cosmological dimming term arises because the radio flux is measured over a finite observing band, rather than bolometrically. The observed flux at a fixed observing frequency $\nu_{\rm obs}$ corresponds to emission at a higher rest-frame frequency $\nu_{\rm em} = (1+z)\nu_{\rm obs}$. For a synchrotron spectrum described by a power law $L_\nu \propto \nu^\alpha$, this introduces a K-correction factor proportional to $(1+z)^\alpha$, which for typical radio sources with $\alpha \simeq -1$ results in an additional suppression of the observed flux by a factor $(1+z)^{-1}$. Moreover, the observed flux is defined as the number of received photons per unit time. Due to cosmological time dilation, the observed time interval is stretched by a factor $(1+z)$ with respect to the emission frame, reducing the photon arrival rate by an additional factor $(1+z)^{-1}$. As a consequence, when considering flux densities measured in a finite frequency band, the observed flux includes an extra cosmological dimming proportional to $(1+z)^{-2}$ in addition to the dependence on D_L. Ultimately, the expected observational radio flux for a simulated source of length L at redshift z is:

$$F_{\rm rad}(z) = F_{\rm ref}\left(\frac{L}{L_{\rm ref}}\right)\left(\frac{D_{\rm L}(z_{\rm ref})}{D_{\rm L}(z)}\right)^2\left(\frac{1+z_{\rm ref}}{1+z}\right)^2 . \tag{2.8}$$

For the high-energy emission, the γ-ray flux (F_γ) originating from the IC scattering of the CMB photons was computed. Theoretically, the ratio between the IC γ-ray flux and the synchrotron radio flux is determined by the ratio of the energy densities of the CMB and the magnetic field

$$\frac{F_\gamma}{F_{rad}} = \frac{U_{\rm CMB}}{U_{\rm B}} . \tag{2.9}$$

An empirically calibrated scaling for this relation was used to generate a prediction in the γ-ray domain. By extracting the values from its spectral energy distribution (Figure 1.5), the reference flux ratio between the expected IC γ-ray emission at 1 GeV in the case of $B = 30\,$nG (in the source reference frame) and the observed synchrotron radio emission at 144 MHz is estimated to be

$$\mathcal{R}_{\rm ref} \sim 6900 .$$

Using this empirical baseline and the local energy densities of the simulated jets, the expected γ-ray flux for each source at redshift z can be calculated:

$$F_\gamma(z) = F_{\rm rad}(z) \times \mathcal{R}_{\rm ref}\left(\frac{U_{\rm CMB}(z)}{U_{\rm CMB,ref}}\right)\left(\frac{U_{\rm B,ref}}{U_{\rm B}(z)}\right) . \tag{2.10}$$

The scaling terms in this equation account for the evolving redshift of my sources: $U_{\mathrm{CMB}}(z) \propto (1+z)^4$ describes the universal cosmological evolution of the CMB photon field, while $U_{\mathrm{B}}(z) = B_{\mathrm{rms}}^2/8\pi$ represents the specific local magnetic energy density, computed directly from the proper root-mean-square magnetic field extracted from the 1D profile of each simulated jet. The reference energy densities, $U_{\mathrm{CMB,ref}}$ and $U_{\mathrm{B,ref}}$, are evaluated with the fiducial Porphyrion values of $z_{\mathrm{ref}} = 0.896$ and $B_{\mathrm{ref}} \approx 30\,\mathrm{nG}$, respectively.

3
Results

In this chapter, I present a comprehensive statistical analysis of the physical and geometrical properties of the simulated jet population. The discussion is structured into three main parts. First, I investigate the fundamental length distributions of the jets across the five simulated redshift snapshots. I analyse the differences between the effective and maximum length metrics, and I evaluate the geometrical impact of converting intrinsic 3D structures into 2D projected observables (Sec. 3.1.1). Second, I present the general demographics obtained by combining the information across all simulated redshift. I show the cumulative number density of the generated structures and subsequently scale these theoretical distributions to predict the total expected all-sky source counts, comparing these predictions with recent observational data (Sec. 3.1.2). Finally, I derive the quantitative predictions for the radio and γ-ray luminosity distributions of the simulated γ-ray beams, evaluating their detectability against current instrumental limits (Sec. 3.2).

3.1 Statistical properties of the simulated jets

3.1.1 Intrinsic distributions and projection effects

As discussed in Section 2.2.2, to construct a statistically significant sample, I executed the ray-tracing routines for $N = 1000$ extractions of jet directions. This approach allows me to study the statistical distribution of the simulated jet lengths, focusing primarily on their sensitivity to different magnetic field thresholds and evaluating the difference between the two metrics that define the size of the emitting structure. Figure 3.1 shows the resulting distribution of the effective (left panels) and maximum (right panels) jet lengths in comoving Mpc, evaluated across five different simulation snapshots from $z = 1.065$ to $z = 0.1$. The histograms are colour-coded based on the assumed comoving magnetic field threshold: 4 nG (blue), 8 nG (red), and 16 nG (yellow). By construction, the upper limit of the distribution is fixed at the comoving length of Porphyrion (13.272 Mpc).

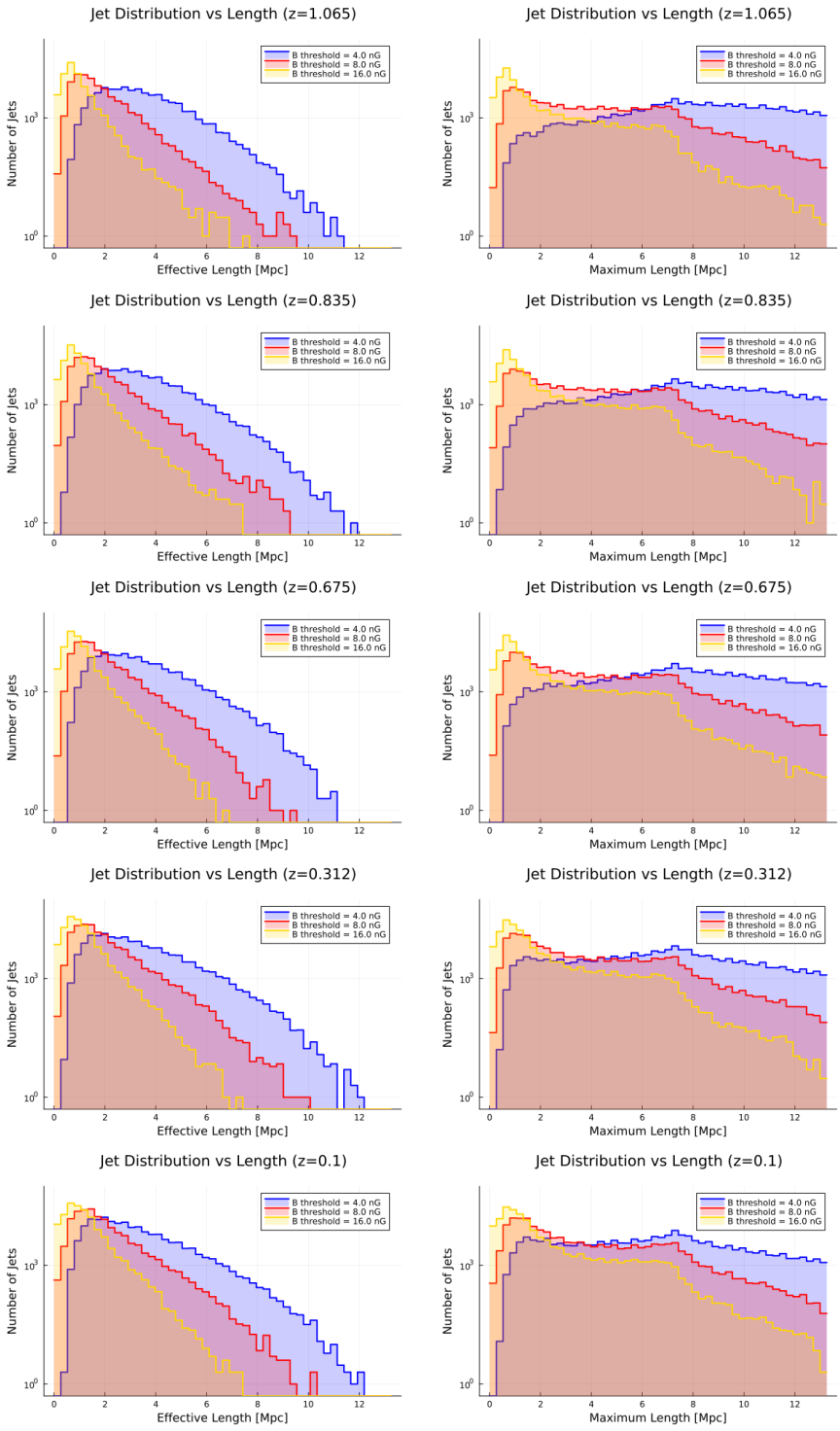

Figure 3.1. Distributions of the effective (left panels) and maximum (right panels) jet lengths in comoving Mpc, derived from 1000 random realizations. The histograms correspond to three distinct comoving magnetic field thresholds: 4 nG (blue), 8 nG (red), and 16 nG (yellow). Rows correspond to simulation snapshots at redshift $z = 1.065,\ 0.835,\ 0.675,\ 0.312$, and 0.1 (from top to bottom).

A comparison between the left and right panels shows a clear difference in the distributions. As expected, since the maximum length is defined through a less restrictive criterion, its distribution is systematically shifted towards larger scales. The effective lengths peak at very short distances ($\sim 1 - 2\,\mathrm{Mpc}$) and decay rapidly, while the maximum lengths exhibit a much broader plateau, extending for several Megaparsecs before dropping. This distinction is observationally relevant: since real giant radio galaxies are frequently observed with significant gaps in surface brightness along their structures, the maximum length provides a realistic observable property. For this reason, it will be employed later in this section to model observable length and luminosity distributions.

Another evident result emerging from Figure 3.1 is the sensitivity of the jet length to the assumed magnetic field strength. When a high threshold is imposed (16 nG yellow histograms), the vast majority of jets have relatively short lengths. In contrast, lowering the threshold to 4 nG (blue histograms) allows the distribution tail to extend to higher lengths. An intermediate situation is observed at the fiducial threshold of 8 nG (red histograms). This results reveal that when jets expand into deep cosmic voids to reach lengths comparable to Porphyrion, they inevitably propagate through regions with very weak magnetisation.

Lastly, by analysing the cosmological evolution from top ($z = 1.065$) to bottom ($z = 0.1$), a subtle trend emerges. In the local Universe, the high-length tail of the effective length distribution appears to be slightly more populated. Initially, this variation could be partially attributed to a statistical sampling bias, given that the number of selected halos in the simulation increases at lower redshift. However, to rigorously test this hypothesis, I performed a consistency check by generating new distributions from a uniform sample of exactly 76 halos for each redshift snapshot. Interestingly, even with this unbiased uniform sampling, a marginal trend towards larger effective lengths in the local Universe remains. This may suggest a potential physical evolution in the local cosmic web environment that might favor the jet observability. For example, the progressive spilling of magnetic field from astrophysical sources, in addition to the primordial magnetic field compressed within filaments, might progressively make it more likely for the γ-ray beams to propagate for longer distances in the low-z Universe.

While the true 3D lengths describe the actual extent of the simulated jets, real astronomical observations are limited to 2D sky projections. This geometrical projection introduces a systematic shift of the entire population towards smaller apparent sizes. To clearly illustrate this effect, Figure 3.2 directly compares the cumulative distributions of the intrinsic (solid lines) and projected (dashed lines) jet lengths. For illustrative

purposes, this comparison focuses on the highest redshift snapshot ($z = 1.065$), since the overall trends remain practically unchanged across different cosmic epochs. Having established this systematic lowering, Figure 3.3 displays the resulting projected distributions for both the effective (left panels) and maximum (right panels) jet lengths across all simulated redshift. These final distributions were obtained by multiplying the intrinsic lengths by $\sin(\theta)$, where the viewing angle θ was extracted from a random isotropic distribution (see Sec. 2.2.4). Consequently, when geometrical projection is included, the fraction of simulated jets that could observationally resemble a Porphyrion-like giant radio galaxy is reduced.

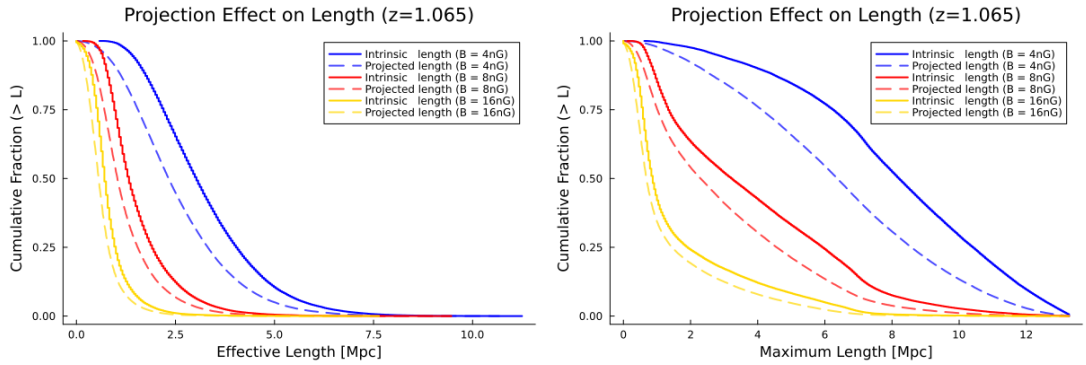

Figure 3.2. Comparison between intrinsic and projected jet length distributions at $z = 1.065$. The left and right panels show respectively the cumulative functions for the effective and maximum lengths in comoving Mpc. Solid curves represent the intrinsic (3D) length, while dashed curves correspond to the projected (2D) length. Colors indicate three distinct comoving magnetic field thresholds: 4 nG (blue), 8 nG (red), and 16 nG (yellow).

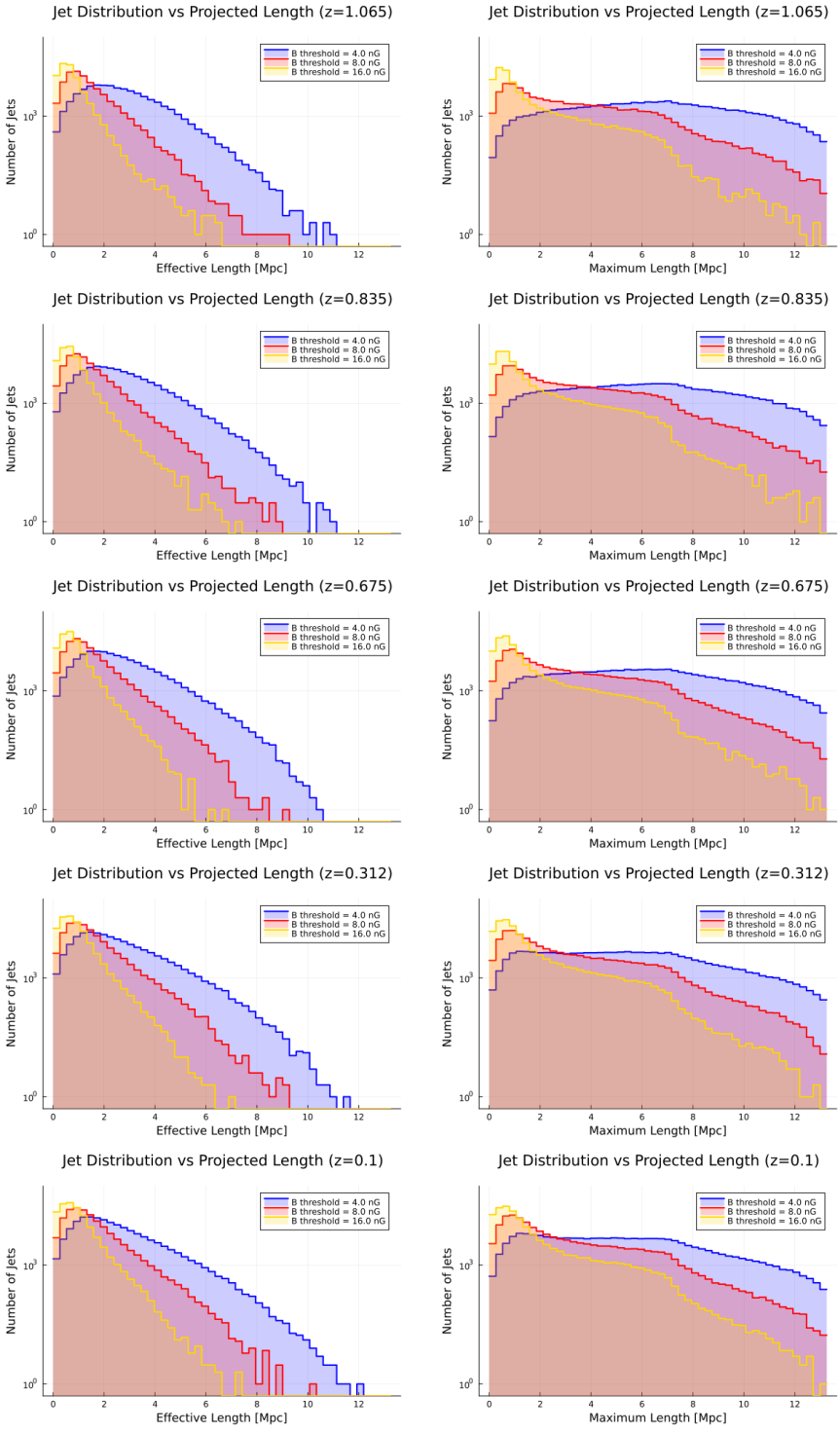

Figure 3.3. Distributions of the projected effective (left panels) and maximum (right panels) jet lengths in comoving Mpc, derived from 1000 random realizations and lines of sight. The histograms correspond to three distinct comoving magnetic field thresholds: 4 nG (blue), 8 nG (red), and 16 nG (yellow). Rows correspond to simulation snapshots at redshift $z = 1.065,\ 0.835,\ 0.675,\ 0.312$, and 0.1 (from top to bottom).

3.1.2 Cumulative statistics and comparison with GRG observations data

From this point on, I shall focus my next results by relying on the maximum projected length metric. Indeed, this is a reasonable way to study jet lengths and potentially compare them to real observations. The intrinsic demographics of the simulated jet population are presented in Figure 3.4. The plots show the cumulative number density of the projected maximum length for both comoving (left column) and physical (right column) scales. The counts are normalized to the volume of the simulation and averaged over the $N = 1000$ random extractions generated in my procedure. The distributions across all simulated redshift are combined and properly weighted by the comoving volume they cover. As expected, cumulative distributions exhibit a monotonically decreasing trend: the population is dominated by smaller structures and sharply drops at extreme lengths. This clearly reflects the physical limitations in reaching enormous dimensions even for γ-ray beams, which are related to the size of long enough filaments in our simulated cosmic web. In fact, the model's requirement to traverse magnetised regions clashes with the increasingly lower probability of encountering long and magnetised enough filaments around halos. This concept becomes even clearer by comparing the different rows, which assume different threshold values for the magnetic field threshold: increasing the comoving threshold from 4 nG to 16 nG systematically lowers the overall number density of the longer structures.

To move from the theoretical simulation to the observable Universe, the volume-weighted all-sky predictions are presented in Figure 3.5. In all the plots the solid blue line represents the simulated all-sky counts. As is clearly visible, this theoretical distribution overestimates the observed population of GRGs from the Andernach & Brüggen (2025) catalog (red markers) by several orders of magnitude. This discrepancy is expected and is a direct consequence of our initial assumption. Indeed, the simulation assumes continuous jet activity for all selected halos, and therefore it represents the total number of structures that could have formed if each SMBH had been constantly active 100% of the time. To account for the AGN duty cycle and to build a realistic model, I have to re-normalise the theoretical counts by the maximum allowed occurrence of these objects based on observations. As described in Section 2.2.5, the simulated curves were downscaled to match the observational data at a reference length of 3 Mpc (indicated by the vertical dashed line). The empirically derived scaling factors for both the comoving and physical length distributions, evaluated across the three magnetic field thresholds, are summarized in Table 3.1. This vertical shift produces the calibrated simulation represented by the green dashed curves.

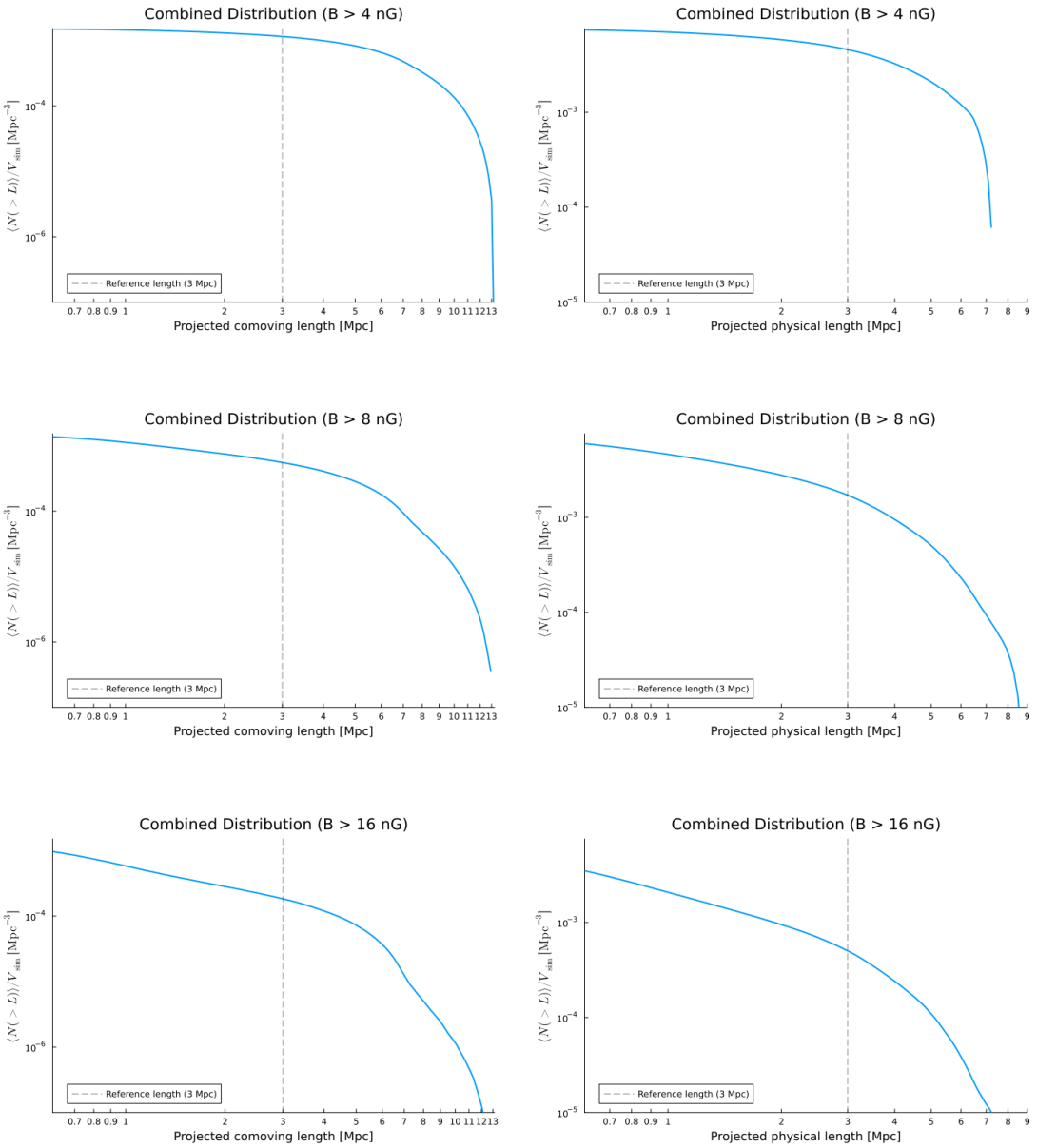

Figure 3.4. Normalized cumulative number density of the projected maximum jet lengths, expressed in comoving (left column) and physical (right column) Mpc. The distributions are pooled across all simulated redshift snapshots (from $z = 0.1$ to $z = 1.065$). The counts are normalized by the comoving volume of the simulation box ($V_{\rm sim} = 42.5^3\,{\rm Mpc}^3$) and averaged over $N = 1000$ random extractions. The rows correspond to the three fiducial magnetic field thresholds: 4 nG (top), 8 nG (middle), and 16 nG (bottom). The vertical dashed line indicates the reference length of 3 Mpc.

Threshold $B_{\rm thr}$	Comoving Scaling Factor	Physical Scaling Factor
4 nG	8.13×10^{-7}	1.18×10^{-6}
8 nG	1.68×10^{-6}	3.91×10^{-6}
16 nG	5.33×10^{-6}	1.72×10^{-5}

Table 3.1. Empirical scaling factors applied to the theoretical all-sky counts to match the observed GRG population at the 3 Mpc reference length. The factors are reported for the three magnetic field thresholds, considering both the comoving and physical length distributions.

The lengths conventionally reported in the observational literature correspond to proper (physical) lengths, hence we focus on the distribution of physical lengths of our objects to derive our main results. A first remarkable result can be noticed: the shape and the slope of the re-calibrated distribution of objects excellently match the observed GRG trend at large scales ($L > 3$ Mpc) from Andernach & Brüggen (2025). This agreement is particularly striking for the 8 and 16 nG comoving magnetic field thresholds, with the 16 nG model providing a near-perfect fit to the high-end tail of the data. Furthermore, below the 3 Mpc threshold, the simulated counts significantly underestimate the observational data. In this regime, the fraction of radio emission produced by γ-ray beams gets increasingly smaller, down to $\sim 2-8\%$ at the smallest lengths (specifically, 2% for the 4 nG threshold, 4.5% for 8 nG, and 8.4% for 16 nG). This discrepancy is entirely consistent with our theoretical framework: the γ-ray beam model is indeed designed to explain the formation of the most extreme giant structures (with mostly rectilinear morphologies) and is not intended to replace standard models for the entire population of radio galaxies and GRGs. Consequently, from these results it appears that γ-ray beam sources could potentially "contaminate" observational surveys by a few percent. However, this implies that a small fraction of the observed large-scale structures assumed to be standard plasma jets, might instead be sustained by this mechanism and produce detectable γ-ray and hard X-ray emission (see next Section).

A final caveat is necessary here: while at the moment this re-calibration process is meant to reproduce the number counts of GRG at a given reference length, using the observational catalog by Andernach & Brüggen (2025), which is the only available one for these extreme sources, such catalog is not complete, and hence the rescaling procedure I used is meant to be a proof of concept, awaiting for more redshift-complete observational catalogs for a more stringent prediction of the γ-ray beam model at all redshift.

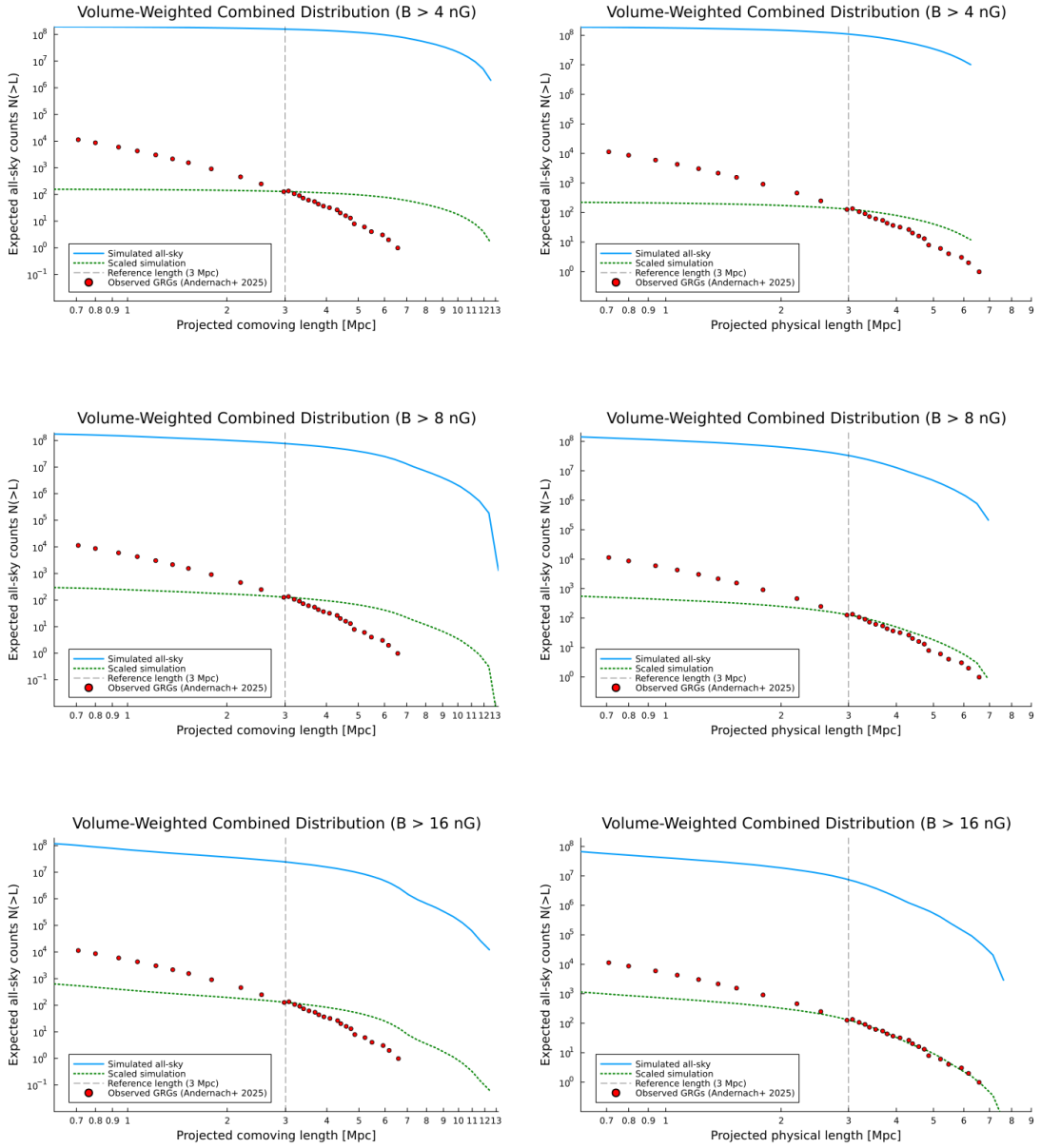

Figure 3.5. Volume-weighted cumulative distributions of expected all-sky source counts as a function of projected comoving (left column) and physical (right column) lengths in Mpc, integrated up to $z = 1.065$. Rows represent magnetic field thresholds of 4 nG (top), 8 nG (middle), and 16 nG (bottom). The solid blue line shows the simulated counts (assuming continuous jet activity). Red markers indicate observed GRGs (Andernach & Brüggen, 2025). The green dashed curve represents the simulation downscaled to match observations at the 3 Mpc reference length (vertical dashed line), effectively accounting for the AGN duty cycle.

3.2 Predictions on the radio and γ-ray luminosity distributions of γ-ray beams

To quantitatively evaluate the detectability of the simulated jet population at higher energies, it is crucial to establish realistic observational thresholds for both the radio and γ-ray regimes.

For the radio band, an empirical estimate of the effective sensitivity for GRGs can be derived directly from the LoTSS GRG sample presented by Dabhade et al. (2020b), who visually identified and characterized GRGs in the LoTSS Data Release 1 maps. In their catalog, the faintest detected GRG have integrated flux densities $F_{144\mathrm{MHz}} \approx 2.5\,\mathrm{mJy} = 2.5 \times 10^{-26}\,\mathrm{erg\,s^{-1}\,cm^{-2}\,Hz^{-1}}$ at 144 MHz, indicating that this value represents a realistic lower detection limit for Mpc–scale radio galaxies in LoTSS data. Assuming an effective observing bandwidth of $\Delta\nu \simeq 48$ MHz for LOFAR high-band antenna, the limiting flux at 144 MHz

$$F_{\mathrm{rad,lim}} = F_{144\,\mathrm{MHz}} \times 4.8 \times 10^{7}\,\mathrm{Hz} \approx 10^{-18}\,\mathrm{erg\,s^{-1}\,cm^{-2}}, \tag{3.1}$$

and I shall use this value as the reference LOFAR sensitivity limit.

Likewise, a sensitivity limit for the high-energy regime must be assumed. The Fermi-LAT detection threshold was extracted directly from the spectral energy distribution (Figure 1.5), resulting in an estimated sensitivity limit for γ-ray emission at 1 GeV of:

$$F_{\gamma,\mathrm{lim}} \approx 5 \times 10^{-13}\,\mathrm{erg\ cm^{-2}s^{-1}}. \tag{3.2}$$

These two thresholds provide the necessary observational boundaries to assess how many of my simulated active sources may be potentially present and detectable by existing (or even future) telescopes.

Before computing the final luminosity distributions, I introduced an additional refinement to the simulated population. In my simulation, the number of selected massive halos naturally increases at lower redshift due to ongoing hierarchical structure formation (see Table 2.2). However, observational studies of the local Universe (van Velzen et al., 2012; Kondapally et al., 2022) demonstrate that the comoving space density of radio AGNs remains roughly constant at $\sim 10^{-3}\,\mathrm{Mpc^{-3}}$ up to $z \approx 1$. To ensure consistency with this observed number density, I introduced a redshift dependent halo mass threshold, tuned to yield exactly 76 candidate halos per snapshot, matching the theoretically expected number of objects within the $(42.5\,\mathrm{Mpc})^3$ simulation volume. This refined sampling progressively reduces the number of simulated objects at low

redshift (by up to a factor of ~ 2) compared to our first estimate. Using both my original simulated population and this uniformly sampled population, I applied the procedure described in Section 2.2.7 for the fiducial comoving magnetic field threshold of 8 nG. The resulting expected all-sky cumulative flux distributions for both the original (solid lines) and the rescaled (dashed lines) population are presented in Figure 3.6. The effect of this second sampling of objects is a minor one, and it only slightly reduces (by a factor ~ 2) the luminosity distributions at both investigated wavelengths, mostly as an effect of the reduction of low-z sources.

The top panel displays the predicted synchrotron radio flux at 144 MHz. The distribution shows that several hundreds to a thousand sources across the entire sky produce an expected radio flux that exceeds the LOFAR sensitivity limit of $\approx 10^{-18}\,\mathrm{erg\,cm^{-2}\,s^{-1}}$. This result confirms that a large fraction of the predicted radio population of γ-ray beams, based on my result, is already detectable at low radio frequency, and therefore that several of already known giant radio galaxies may be ascribed to the mechanism investigated in my Thesis. Considering the entire predicted distribution within $z \leq 1$, approximately $\sim 10^2$ objects should be more luminous than $10^{-16}\,\mathrm{erg\ cm^{-2}\ s^{-1}}$ at 144 MHz. This is important because it can motivate the further detailed testing of a few known GRG under the assumption of the γ-ray beam model for radio emission, and put it under a more stringent and object-by-object scrutiny.

On the other hand, much fewer objects from the same distribution are predicted to be detectable in the γ-ray window, given the Fermi-LAT's sensitivity. The bottom panel shows the corresponding inverse Compton γ-ray flux at 1 GeV. The resulting flux distribution drops off more steeply than its radio counterpart. This is because the expected IC flux scales with the local magnetic energy density. Specifically, a stronger magnetic field implies a higher U_B, which in turn predicts a lower γ-ray flux, as expressed by Equation (1.3). Nevertheless, the model predicts that a small sample (~ 10) of these sources, is capable of exceeding the Fermi-LAT detection limit of $\approx 5 \times 10^{-13}\,\mathrm{erg\,cm^{-2}\,s^{-1}}$). This is an intriguing result, because it indicates that the largest AGN jets, under favorable physical conditions, could also be detectable as γ-ray emitters.

To better investigate the physical and cosmological origins of the brightest sources, I decomposed the total cumulative flux distributions into discrete bins of length and redshift. It is important to note that, to produce these binned distributions, I utilized the rescaled simulated population. As introduced previously, this population was downsampled to maintain a constant comoving density of active sources ($\sim 10^{-3}\,\mathrm{Mpc^{-3}}$, corresponding to exactly 76 halos per snapshot). This normalization is crucial when

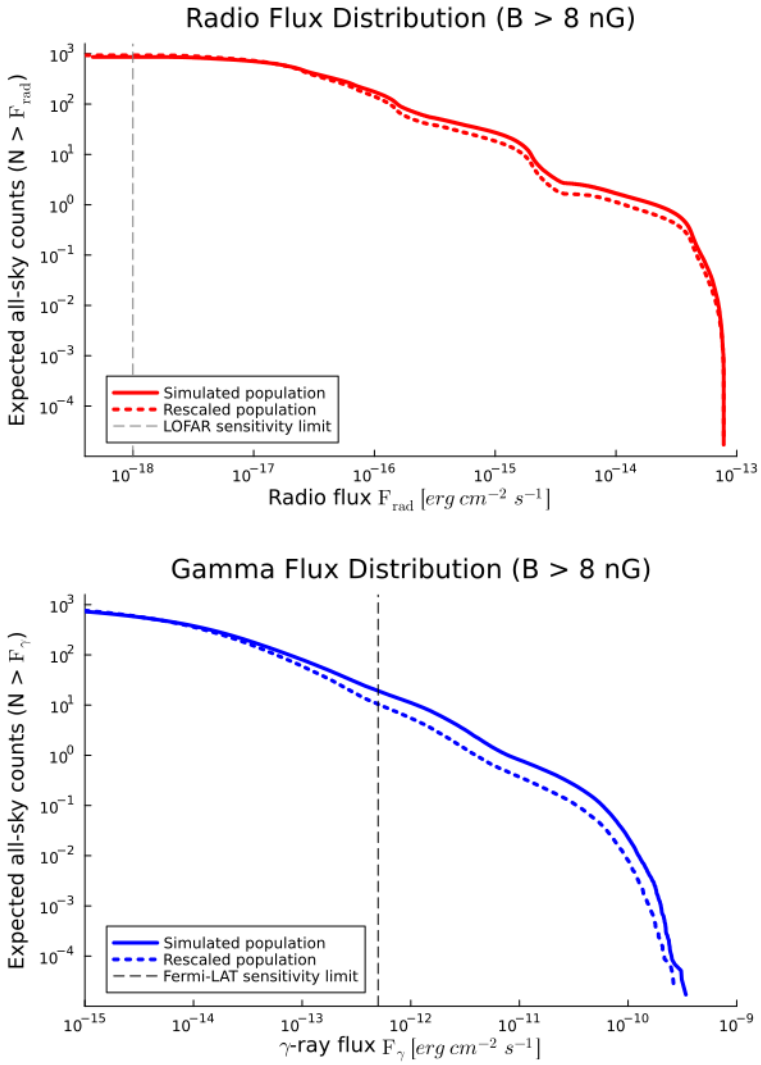

Figure 3.6. Expected all-sky cumulative flux distributions for the simulated jet population, evaluated for the comoving magnetic field threshold of 8 nG. In both panels, the solid curves represent the fluxes derived from the simulated population, while the dashed curves correspond to the rescaled population, downsampled to maintain a constant comoving density of active sources ($\sim 10^{-3}\,\mathrm{Mpc}^{-3}$, corresponding to 76 halos per snapshot). The top panel represents the predicted synchrotron radio flux at 144 MHz. The vertical dashed line indicates the approximate sensitivity limit of the LOFAR survey ($\approx 10^{-18}\,\mathrm{erg\,cm^{-2}\,s^{-1}}$). The bottom panel shows the predicted inverse Compton γ-ray flux at 1 GeV, derived by scaling the radio emission according to the local magnetic and CMB energy densities. The vertical dashed line denotes the Fermi-LAT sensitivity limit ($\approx 5 \times 10^{-13}\,\mathrm{erg\,cm^{-2}\,s^{-1}}$).

binning by redshift, as it prevents an artificial overabundance of local structures and ensures that the results reflect physical and cosmological trends.

First, I investigated the dependency of the fluxes on the physical extent of the sources. The resulting length-binned distributions are shown in Figure 3.7. The top and bottom panels show the radio and γ-ray flux distributions, respectively, binned by their lengths ($L < 3\,\mathrm{Mpc}$, $3 \leq L \leq 7\,\mathrm{Mpc}$, and $L > 7\,\mathrm{Mpc}$). In both observing bands, the high-flux tails of the distributions are dominated by the most extended structures ($L > 7\,\mathrm{Mpc}$, blue dashed curves). In contrast, smaller structures ($L < 3\,\mathrm{Mpc}$) have lower fluxes. This behaviour is easily understood as a direct consequence of the physical assumption of the model, where the intrinsic emission is set to scale linearly with the physical length of the active jet.

Next, I evaluated the impact of the redshift of the host halos on the observable flux. These results are presented in Figure 3.8. The data are divided into 5 intervals based on the snapshot redshift (from $z = 0.1$ to $z = 1.065$). The plots show how the extreme emitters, both in radio (top panel) and in γ-rays (bottom panel), are objects at low redshift ($z = 0.1$, yellow dashed curves), but in any case the number of objects is small. As the redshift increases, the curves progressively shift toward lower fluxes. This is a direct effect of the strong cosmological dimming described in Section 2.2.7, where the combination of the luminosity distance D_L^2 and the additional $(1+z)^{-2}$ surface brightness factor severely attenuates the observed fluxes of the high-z population.

Overall, the two sensitivities considered here for LOFAR and Fermi-LAT, combined with the previous scalings, show that the bulk of potentially detectable objects in the two observational frequencies are significantly different: the bulk of the detectable population at radio wavelengths is made by "short" (≤ 3 Mpc) and high-redshift ($z \geq 0.5$) sources, while the bulk of the population detectable in γ-rays is made by longer ($\sim 3 - 7$ Mpc) and more local ($z \leq 0.3$) objects.

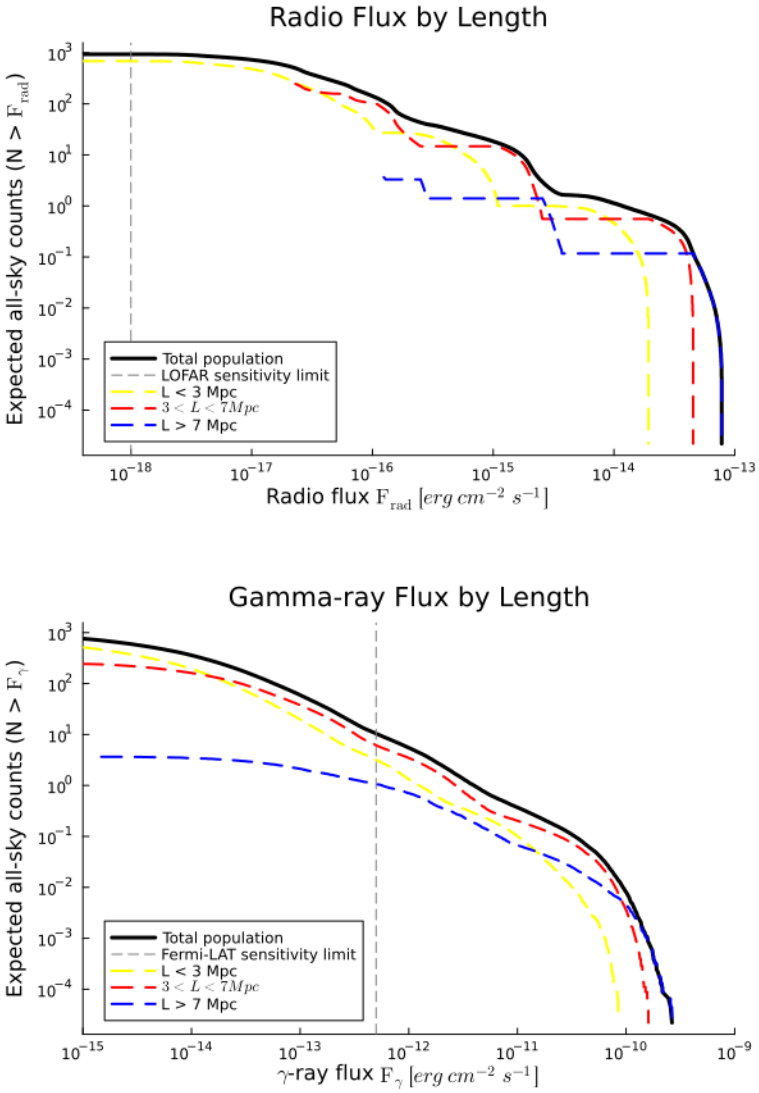

Figure 3.7. Predicted all-sky flux distributions (for the 8 nG comoving threshold) binned by the physical length of the jets ($L < 3$ Mpc, $3 \leq L \leq 7$ Mpc, and $L > 7$ Mpc). The top and bottom panels show the radio (144 MHz) and γ-ray (1 GeV) fluxes, respectively. The data are derived from the rescaled population (matching exactly 76 halos per snapshot) in order not to over-estimate the abundance of galaxies potentially hosting γ-ray beams, based on the known abundance of radio galaxies in the local Universe. The solid black line in both panels represents the total cumulative distribution. These distributions illustrate how the high-flux tails are predominantly driven by the most extended sources.

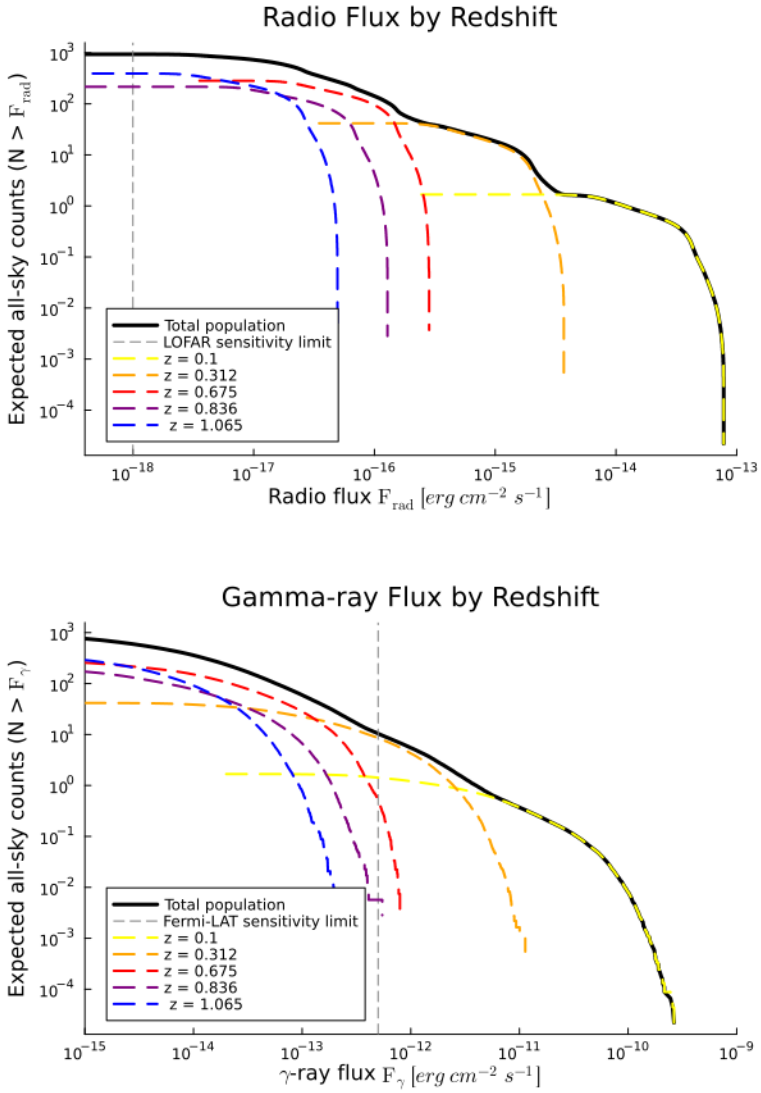

Figure 3.8. Predicted all-sky flux distributions (for the 8 nG comoving threshold) binned by the cosmological redshift of the simulation snapshots. The top and bottom panels show the radio (144 MHz) and γ-ray (1 GeV) fluxes, respectively. The data are derived from the rescaled population (matching exactly 76 halos per snapshot) in order not to over-estimate the abundance of galaxies potentially hosting γ-ray beams, based on the known abundance of radio galaxies in the local Universe. The solid black line in both panels represents the total cumulative distribution. These plots illustrate the strong effect of cosmological dimming, which severely attenuates the fluxes of the higher-z populations.

4

Discussion and Conclusions

In this Thesis, I explored the observational and statistical implications of an alternative explanation for the formation of the most extreme Giant Radio Galaxies in the Universe, which was motivated by the recent discovery of the 7 Mpc long Porphyrion system. The existence of objects like Porphyrion challenges our basic understanding of the formation and propagation of jets on extragalactic scales, considering the large energetic demands, the apparent lack of interaction with the external medium and of precession of their supermassive black hole of origin (which shows basically no precession on scales of $\sim 1-2$ Gyr) as well as their anomalous stability against the internal magnetohydrodynamic instabilities which are expected in standard radio jets. Therefore, with this Thesis I quantitatively tested the viability of the **gamma-ray beam model** proposed by Neronov et al. (2025), an alternative explanation for the formation of Porphyrion and other similar objects, which might avoid the physical anomalies arising in the standard jet model. According to this model, the radio jet-like structure may actually be produced by a beam of very high-energy γ-rays. As these photons propagate, they interact with the extragalactic background light to produce secondary electron-positron pairs. Whenever these secondary pairs are deposited along the beam's path while this crosses the intergalactic medium of cosmic filaments, the magnetic field which they encounter may be large enough to make them detectable in the radio band (via synchrotron emission) and in the hard X-ray and γ-ray bands (via inverse Compton emission).

Assessing whether this mechanisms can really work and computing a fraction of GRGs which may realistically be produced by this scenario is important, both to improve our understanding of the high energy processes linked to the evolution of AGNs, as well as to assess the actual role played by GRGs in the magnetisation of the Universe on large scale. The latter would obviously be different, if all observed radio jets are high velocity magnetised plasma lobes ejected into voids (in which case the predicted magnetisation of cosmic voids by astrophysical seeding is large), or else if they are photon beams not carrying any magnetic field outside of their host halos, but rather they illuminate magnetic fields in filaments (which are mostly of a primordial origin in our model).

To test this scenario in detail, I developed new numerical routines to evaluate in a

statistical way the formation and the radiative properties of radio jets produced by γ-ray beams, using pre-existing state-of-the-art cosmological simulations of the intergalactic environment. Below is a schematic summary of the scientific case, the methodology and the main findings of this work, followed by a detailed discussion of their physical implications and future perspectives.

4.1 Methods and Results

My Thesis work is aimed to investigate, for the first time, the γ-ray beam model in a statistical way, and using state-of-the-art cosmological simulation to assess which fraction of observed GRGs might be realistically be ascribed to this mechanism. This study also makes it possible to test, for the first time, how this proposed mechanism to mimic GRGs compare with available power and size distributions of known radio sources.

- **Environmental extraction from cosmological simulations:** Using cosmological ENZO-MHD simulations, I extracted thousands of one-dimensional profiles starting from a selected sample of galactic halos and extending along random directions to match the total length of Porphyrion. This procedure was repeated across five redshift (from $z = 0.1$ to $z = 1.065$), to assess the impact of cosmic evolution. These 1D trajectories are intended to simulate the physical conditions along the propagation path of a random-oriented relativistic jet from a SMBH. Each jet accurately traces the baryonic density, the temperature, and, most importantly, the **magnetic field** that the γ-ray beam would traverse. This was used to define the size and radiative properties of the simulated jets, assuming different magnetic field thresholds, which physically represent the minimum environmental magnetisation required for the secondary pairs to produce a detectable synchrotron radio flux as discussed in Neronov et al. (2025).

- **All-sky extrapolation and empirical calibration:** The simulation covers a finite comoving volume ($42.5^3\,\mathrm{Mpc}^3$), hence I had to extrapolate the simulated jet population to the entire sky and to appropriately apply redshift-dependent corrections, in order to compare with real catalogs of GRGs, after a proper rescaling to compare with the known demographics of GRG at the reference length of 3 Mpc.

- **Radiative modelling:** I computed the expected radio and γ-ray emission for each simulated structure, predicting luminosity distributions of γ-ray beams, assuming

a physical scaling calibrated with the observed properties of Porphyrion.

Main Results:

- **Largest GRGs:** The full-sky distribution of the simulated observable lengths, after calibrating for the abundance of radio galaxies in the local Universe, reproduces well the observed GRG trend for lengths $L > 3\,\mathrm{Mpc}$. This agreement is remarkably tight when comoving magnetic field thresholds of 8 and 16 nG are assumed. Furthermore, aligning the theoretical population with the observations required a downscaling factor of $\sim 10^{-6}$. This parameter effectively acts as an empirical duty cycle, strongly indicating that the emission of powerful, megaparsec-scale γ-ray beams is an extremely rare phase of activity for the supermassive black holes hosted in the selected halos.

- **Smallest GRGs:** For structures smaller than 3 Mpc, the model significantly underestimates the observational data. This also is a good result as the bulk of the known radio galaxy population is not made by extremely rectilinear jets as Porphyrion. This confirms that the vast majority of known GRGs is contributed by radio jets formed as in the standard scenario. The γ-ray beam model was specifically designed to explain the formation of the most extreme and peculiar giant structures (with mostly rectilinear morphologies), but it cannot replace standard MHD models for the entire population of radio galaxies and GRGs. In detail, my results suggest that γ-ray beam-driven sources constitute only a minor sub-population that potentially "contaminates" standard radio catalogs by mimicking classical plasma jets. Hence a small fraction ($\sim 2 - 8\%$) of observed GRGs, with rectilinear morphologies, is predicted by this model to be produced by the γ-ray beam mechanism, making such sources prime candidates for detectable γ-ray and hard X-ray emission.

- **Detectability Predictions:** The predictions regarding the radio (at 144 MHz) and γ-ray (at 1 GeV) flux distributions yield additional important findings. A large fraction of the predicted radio population produced by γ-ray beams should be already detectable at low radio frequencies, suggesting that several of the currently known GRGs may actually be ascribed to this mechanism. Considering the entire predicted distribution up to $z \leq 1$, approximately $\sim 10^2$ objects should exhibit a radio flux greater than $10^{-16}\,\mathrm{erg\,cm^{-2}\,s^{-1}}$ at 144 MHz. On the other hand, the detectability in γ-rays is predicted to be limited to ~ 10 objects across the entire sky, up to $z \sim 1$. In both the radio and γ-ray bands, the high-flux tails

of the distributions are dominated by the most extended sources. The comparison with the LOFAR and Fermi-LAT sensitivities reveals that the bulk of potentially detectable objects in these two observational windows possess significantly different characteristics. The detectable radio population is primarily composed of "shorter" ($\leq 3\,\mathrm{Mpc}$) and higher-redshift ($z \geq 0.5$) sources, whereas the population detectable in γ-rays is dominated by longer ($\sim 3 - 7\,\mathrm{Mpc}$) and more local ($z \leq 0.3$) objects.

4.2 Implications and future perspectives

The results of my Thesis overall **reinforce the validity of the γ-ray beam model**. The promisingly good agreement between the calibrated simulation and the observational statistics of GRGs with length $> 3\,\mathrm{Mpc}$ demonstrates that the interplay between beams of γ-rays and the cosmic web simulated in a realistic simulation can overall produce a population of rectilinear radio emitting structures with the correct distribution of power and projected lengths, which is a non-trivial result. Furthermore, neither the small-scale statistics nor the detectability predictions yield any evidence that rules out this scenario. Of course, this result depends on the assumed primordial magnetic field scenario for cosmic magnetism. If magnetic fields in the cosmic web are entirely of astrophysical origin, then the same γ-ray beam model would produce no extended radio structures at all. However, the primordial magnetic field model used in these simulations is presently the one yielding the best comparison with observed Faraday Rotation and synchrotron stacking data (e.g. Carretti & Vazza (2025) and references therein), which also seems to reject the possibility that large scale extragalactic magnetic fields can be solely of astrophysical origin, also considering the lower limits on the magnetisation of voids ($\geq 10^{-17} - 10^{-16}$G) derived from the non-detection of inverse Compton Cascade emission from blazars (e.g. Neronov & Vovk, 2010; Alves Batista & Saveliev, 2021).

Regarding the empirical duty cycle derived from the calibration, the obtained value of $\sim 10^{-6}$ appears exceptionally low when compared to the typical $1 - 2\%$ "on-time" fraction estimated for the general blazar population (Yoshida et al., 2023). While comparing general blazars to the specific (and currently unconstrained) duty cycle of TeV-emitting AGNs requires caution, it can give us an idea of the effective frequency for the production of extreme γ-ray jets. The small value obtained in this work can be explained by a combination of physical and methodological factors. Physically, it reflects the extreme rarity of prolonged TeV AGN flaring events capable of sustaining such giant structures. Methodologically, the normalization factor might be pushed to lower values by observational biases, as I relied on a single, potentially incomplete

catalog for sources at $z < 1$. Moreover, in my model I assumed that all halos above a given mass could potentially host a beam of $\sim$ TeV photons, without any distinction based on the galaxy host morphology or mass accretion histories (both of which could not be reliably measured in the simulation due to resolution limitations). Additionally, the metric used in the Thesis to measure lengths might numerically overestimate the intrinsic population of GRGs. However, while these factors affect the duty cycle, they do not alter the trend of the distribution, preserving the physical robustness of the large-scale match.

The results of my Thesis also **suggest more statistical tests to validate or reject the γ-ray beam model, using radio and γ-ray observations**. Indeed the forward-modeling of the radio and γ-ray flux distributions yields observational indications to test this model and identify new candidates beyond Porphyrion in real survey data. My results indicate that approximately 10^2 sources should exhibit a radio radio flux exceeding $10^{-16}\,\mathrm{erg\,cm^{-2}\,s^{-1}}$ at 144 MHz. i.e. at frequencies which can already be tested with LOFAR. This represents a fundamental finding, as it motivates the detailed re-evaluation of a subset of already known GRGs under the γ-ray beam hypothesis, subjecting them to rigorous, object-by-object scrutiny. Looking ahead, my Thesis predicts a clear difference between the properties of detectable γ-ray powered beam jets which should be detectable in surveys: future radio surveys are expected to discover these sources predominantly at higher redshifts ($z \geq 0.5$), while most chances for γ-ray detections are for the largest ($3 - 7\,\mathrm{Mpc}$) and more local ($z \leq 0.3$) systems.

An additional observational prediction that I have not explored in this work concerns the inverse Compton emission produced by secondary electrons in the jet. In particular, GeV-energy electrons are expected to persist in the jet because of their relatively long cooling timescales. These particles would up-scatter ambient photons, producing emission in the hard X-ray band, around $E \sim 100\,\mathrm{keV}$. If the activity timescale of the γ-ray beam from the parent AGN extends to $\gtrsim 100$ Myr, electrons could cool to sub-GeV energies and generate inverse Compton emission in the softer X-ray band, where present X-ray telescopes might have sufficient sensitivity to detect such a signal.

To expand and refine the study initiated with this Thesis, several aspects could still be improved. Future modelling attempts should move from the current 1D approximation I used here, towards full 3D simulations of the jets. In this way, simulations will better account for the complex geometry of the magnetised medium and make more realistic predictions of the luminosity distributions. However, a detailed spectral modelling of the radio emitting electrons and positrons, in the sense to allow that to also propagate off-axis with respect to main direction of the photon beam, should be implemented as

well. Instead of estimating radio and γ-ray fluxes using simplified scaling relationships as in this work, the broad-band spectral energy distribution could be computed more in detail, also accounting for the time-dependent injection and cooling of the electrons and positrons along the photon beam. This would provide more stringent observational implications: for instance, it will naturally yield the expected level of hard X-ray inverse Compton emission, which might be observable with existing X-ray telescopes (e.g. XMM-Newton).

Together, these improvements will help building a more complete picture of the γ-ray beam model, of its observational implications, and suggest new ways to further constrain it from the observational viewpoint.

A

Appendix

This appendix provides a sample numerical routine, written in the Julia programming language, which I wrote to perform the 1D environmental extraction from the 3D cosmological simulations, as described in Section 2.2.2. The script is designed to systematically trace the paths of the simulated γ-ray beams originating from the centres of selected massive host halos ($M_{200} > 10^{12}\,M_{\odot}$). By iterating over $N = 1000$ randomized lines of sight, the code reads the 3D grid data (density, temperature, and magnetic field components) from the HDF5 snapshot files and computes the profiles along the jet trajectories, applying the appropriate unit conversions and the periodic boundary conditions. These extracted profiles provide the core dataset required to perform the statistical analysis, the radiative forward-modeling, and the detectability predictions presented in Chapter 3.

Extraction of 1D halo profiles from the simulation snapshot.

```
using HDF5, DelimitedFiles, JLD2

"""Structure storing a 1D halo profile extracted along a random line."""
struct HaloProfile
    dist::Vector{Float64}   # distance from halo center
    dens::Vector{Float64}   # gas density
    temp::Vector{Float64}   # temperature
    B::Vector{Float64}      # magnetic field magnitude
    R200::Float64           # virial radius (grid units)
    extraction::Int         # extraction index
    theta::Float64          # polar angle
    phi::Float64            # azimuthal angle
    id_halo::Int            # halo index in catalog
end


"""
Extract density, temperature and |B| profiles along a line
passing through the halo center with direction (theta,phi).
"""
function
    halo_profile_1D(D_ds,T_ds,Bx_ds,By_ds,Bz_ds,data,cdd::Float64,cb::Float64,
                        ihalo::Int,N::Int,L::Float64,theta::Float64,
                        phi::Float64,R_max_Mpc::Float64)

    x_halo,y_halo,z_halo,R200_halo = data[ihalo,1:4]      # halo position + R200
    scale = N/L                                           # Mpc --> grid cells
```

```
    R200_halo_cells = R200_halo*scale

    P0 = [x_halo,y_halo,z_halo]                          # halo centre (Mpc)

    @fastmath u = [sin(theta)*cos(phi),                  # unit direction vector
                   sin(theta)*sin(phi),
                   cos(theta)]

    npts = round(Int,2*R_max_Mpc*scale)                  # number of samples
    ts = range(-R_max_Mpc,R_max_Mpc;length=npts).*scale  # line parameter

    local_dist = collect(ts)
    local_dens = zeros(Float64,npts)
    local_temp = zeros(Float64,npts)
    local_Bmod = zeros(Float64,npts)

    @inbounds for i in 1:npts

        pos = P0.*scale .+ ts[i].*u                      # position along line
        ix,iy,iz = trunc.(Int,pos .+ 0.5)                # nearest grid cell

        # periodic boundary conditions
        if ix<1; ix=N+ix-1; elseif ix>N; ix=ix-N+1; end
        if iy<1; iy=N+iy-1; elseif iy>N; iy=iy-N+1; end
        if iz<1; iz=N+iz-1; elseif iz>N; iz=iz-N+1; end

        # read simulation fields
        d  = D_ds[ix,iy,iz]
        T  = T_ds[ix,iy,iz]
        bx = Bx_ds[ix,iy,iz]; by = By_ds[ix,iy,iz]; bz = Bz_ds[ix,iy,iz]

        # apply unit conversion
        local_dens[i] = d*cdd
        local_temp[i] = T
        local_Bmod[i] = sqrt(bx^2+by^2+bz^2)*cb
    end

    return local_dist,local_dens,local_temp,local_Bmod,R200_halo_cells
end


# ---------------- Simulation parameters ----------------

N = 1024;  L = 42.5;  z = 1.065                      # grid, box size, redshift

# ---------------- Unit conversions ----------------

cdd_proper = 2.82e-30*(1+z)^3;  cdd_comoving = 2.82e-30
cv = 1.258e9
cb_proper = sqrt(cdd_comoving*4  )*cv*(1+z)^2
cb_comoving = sqrt(cdd_comoving*4  )*cv

```

```
proper = false
cdd = proper ? cdd_proper : cdd_comoving                # choose units
cb  = proper ? cb_proper  : cb_comoving


# ---------------- Input files ----------------

simulation_snapshot = "PATH_TO_SIMULATION_SNAPSHOT"     # HDF5 snapshot
halos_catalog       = "PATH_TO_HALO_CATALOG"            # halo catalog

data = readdlm(halos_catalog)                           # load halo table
x_halo = data[:,1];  M200_tot = data[:,5]

R_max_Mpc_comoving = 6.636


# ---------------- Extraction setup ----------------

N_extraction = 1000
nhalos = length(x_halo)

theta = zeros(Float64,N_extraction)
phi   = zeros(Float64,N_extraction)

profiles = HaloProfile[]                                # output container
indici = Int[]


# ---------------- Profile extraction ----------------

h5open(simulation_snapshot,"r") do file_handle

    D_ds = file_handle["Density"];  T_ds = file_handle["Temperature"]
    Bx_ds = file_handle["Bx"];      By_ds = file_handle["By"];   Bz_ds =
        file_handle["Bz"]

    for estrazione in 1:N_extraction

        theta[estrazione] =   *rand()                   # random direction
        phi[estrazione]   = 2  *rand()

        for ihalo in 1:nhalos

            if M200_tot[ihalo] > 1e12                   # halo mass threshold

                push!(indici,ihalo)

                dist,dens_jet,temp_jet,B_jet,R200_jet =
                    halo_profile_1D(D_ds,T_ds,Bx_ds,By_ds,Bz_ds,
                                    data,cdd,cb,ihalo,N,L,
                                    theta[estrazione],phi[estrazione],
                                    R_max_Mpc_comoving)
```

```
130
131                 push!(profiles,HaloProfile(dist,dens_jet,temp_jet,B_jet,
132                                            R200_jet,estrazione,
133                                            theta[estrazione],phi[estrazione],
134                                            ihalo))
135             end
136         end
137     end
138 end
139
140
141 # ---------------- Save results ----------------
142
143 @save "results_1000_extractions.jld2" profiles theta phi
```

Bibliography

Aghanim, N., Akrami, Y., Ashdown, M., et al. 2020a, Astronomy amp; Astrophysics, 641, A6, doi: 10.1051/0004-6361/201833910

—. 2020b, Astronomy amp; Astrophysics, 641, A6, doi: 10.1051/0004-6361/201833910

Aharonian, F., Akhperjanian, A. G., Bazer-Bachi, A. R., et al. 2006, , 440, 1018, doi: 10.1038/nature04680

Alves Batista, R., & Saveliev, A. 2021, Universe, 7, 223, doi: 10.3390/universe7070223

Andernach, H., & Brüggen, M. 2025, , 699, A257, doi: 10.1051/0004-6361/202452961

Anderson, C. S., McClure-Griffiths, N. M., Rudnick, L., et al. 2024, MNRAS, 533, 4068, doi: 10.1093/mnras/stae1954

Antonucci, R. 1993, , 31, 473, doi: 10.1146/annurev.aa.31.090193.002353

Barthel, P. D. 1989, , 336, 606, doi: 10.1086/167038

Beckmann, V., & Shrader, C. R. 2013, The AGN phenomenon: open issues. https://arxiv.org/abs/1302.1397

Bertone, S., Vogt, C., & Enßlin, T. 2006, , 370, 319, doi: 10.1111/j.1365-2966.2006.10474.x

Bicknell, G. V. 1995, The Astrophysical Journal Supplement Series, 101, 29, doi: 10.1086/192232

Biteau, J., Prandini, E., Costamante, L., et al. 2020, Nature Astronomy, 4, 124, doi: 10.1038/s41550-019-0988-4

Blandford, R. D., & Znajek, R. L. 1977, Monthly Notices of the Royal Astronomical Society, 179, 433, doi: 10.1093/mnras/179.3.433

Bonafede, A., Feretti, L., Murgia, M., et al. 2010, Astronomy and Astrophysics, 513, A30, doi: 10.1051/0004-6361/200913696

Bondarenko, K., Boyarsky, A., Korochkin, A., et al. 2022, , 660, A80, doi: 10.1051/0004-6361/202141595

Capetti, A., Massaro, F., & Baldi, R. D. 2017, AA, 601, A81, doi: 10.1051/0004-6361/201630247

Carretti, E., & Vazza, F. 2025, Universe, 11, 164, doi: 10.3390/universe11050164

Carretti, E., Vazza, F., O'Sullivan, S. P., et al. 2024, arXiv e-prints, arXiv:2411.13499, doi: 10.48550/arXiv.2411.13499

—. 2025, , 693, A208, doi: 10.1051/0004-6361/202451333

Chiaberge, M., Macchetto, F. D., Sparks, W. B., et al. 2002, , 571, 247, doi: 10.1086/339846

Costamante, L., Ghisellini, G., Giommi, P., et al. 2001, A&A, 371, 512, doi: 10.1051/0004-6361:20010412

Dabhade, P., Saikia, D. J., & Mahato, M. 2023, Journal of Astrophysics and Astronomy, 44, 13, doi: 10.1007/s12036-022-09898-5

Dabhade, P., Mahato, M., Bagchi, J., et al. 2020a, , 642, A153, doi: 10.1051/0004-6361/202038344

Dabhade, P., Röttgering, H. J. A., Bagchi, J., et al. 2020b, , 635, A5, doi: 10.1051/0004-6361/201935589

Donnert, J., Vazza, F., Brüggen, M., & ZuHone, J. 2018, , 214, 122, doi: 10.1007/s11214-018-0556-8

Donnert, J., Vazza, F., Brüggen, M., & ZuHone, J. 2018, Space Science Reviews, 214, doi: 10.1007/s11214-018-0556-8

Ellis, J., Fairbairn, M., Lewicki, M., Vaskonen, V., & Wickens, A. 2019, Journal of Cosmology and Astroparticle Physics, 2019, 019, doi: 10.1088/1475-7516/2019/09/019

Fanaroff, B. L., & Riley, J. M. 1974, , 167, 31P, doi: 10.1093/mnras/167.1.31P

Ferrière, K., West, J. L., & Jaffe, T. R. 2021, Monthly Notices of the Royal Astronomical Society, 507, 4968, doi: 10.1093/mnras/stab1641

Fidler, C., Pettinari, G., & Pitrou, C. 2016, Phys. Rev. D, 93, 103536, doi: 10.1103/PhysRevD.93.103536

Finke, J. D., Razzaque, S., & Dermer, C. D. 2010, , 712, 238, doi: 10.1088/0004-637X/712/1/238

Fitoussi, T., Belmont, R., Malzac, J., et al. 2017, Monthly Notices of the Royal Astronomical Society, 466, 3472, doi: 10.1093/mnras/stw3365

Fujita, T., Namba, R., Tada, Y., Takeda, N., & Tashiro, H. 2015, Journal of Cosmology and Astroparticle Physics, 2015, 054–054, doi: 10.1088/1475-7516/2015/05/054

Furlanetto, S. R., & Loeb, A. 2001, , 556, 619, doi: 10.1086/321630

Gaspari, M., Eckert, D., Ettori, S., et al. 2019, ApJ, 884, 169, doi: 10.3847/1538-4357/ab3c5d

Govoni, F., Dolag, K., Murgia, M., et al. 2010, AA, 522, A105, doi: 10.1051/0004-6361/200913665

Hardcastle, M., & Croston, J. 2020, New Astronomy Reviews, 88, 101539, doi: 10.1016/j.newar.2020.101539

Hardcastle, M. J., Alexander, P., Pooley, G. G., & Riley, J. M. 1998, , 296, 445, doi: 10.1046/j.1365-8711.1998.01480.x

Hardcastle, M. J., Evans, D. A., & Croston, J. H. 2009, , 396, 1929, doi: 10.1111/j.1365-2966.2009.14887.x

Hardcastle, M. J., Horton, M. A., Williams, W. L., et al. 2023, , 678, A151, doi: 10.1051/0004-6361/202347333

Hogg, D. W. 2000, Distance measures in cosmology. https://arxiv.org/abs/astro-ph/9905116

Hutschenreuter, S., Dorn, S., Jasche, J., et al. 2018, Classical and Quantum Gravity, 35, 154001, doi: 10.1088/1361-6382/aacde0

Kennicutt, Jr., R. C. 1998, ApJ, 498, 541, doi: 10.1086/305588

Kondapally, R., Best, P. N., Cochrane, R. K., et al. 2022, Monthly Notices of the Royal Astronomical Society, 513, 3742–3767, doi: 10.1093/mnras/stac1128

Kravtsov, A. V. 2003, ApJL, 590, L1, doi: 10.1086/376674

Laing, R. A., Jenkins, C. R., Wall, J. V., & Unger, S. W. 1994, in Astronomical Society of the Pacific Conference Series, Vol. 54, The Physics of Active Galaxies, ed. G. V. Bicknell, M. A. Dopita, & P. J. Quinn, 201

Longair, M. S. 2011, High Energy Astrophysics, 3rd edn. (Cambridge University Press)

Matarrese, S., Mollerach, S., Notari, A., & Riotto, A. 2005, Physical Review D, 71, doi: 10.1103/physrevd.71.043502

Mingo, B., Croston, J. H., Hardcastle, M. J., et al. 2019, Monthly Notices of the Royal Astronomical Society, 488, 2701, doi: 10.1093/mnras/stz1901

Mostert, R. I. J., Oei, M. S. S. L., Barkus, B., et al. 2024, , 691, A185, doi: 10.1051/0004-6361/202348897

Mostert, R. I. J., Oei, M. S. S. L., Barkus, B., et al. 2024, Astronomy amp; Astrophysics, 691, A185, doi: 10.1051/0004-6361/202348897

Neronov, A., Vazza, F., Brandenburg, A., & Caprini, C. 2025, , 696, L8, doi: 10.1051/0004-6361/202453099

Neronov, A., & Vovk, I. 2010, Science, 328, 73, doi: 10.1126/science.1184192

Oei, M. S. S. L., van Weeren, R. J., Gast, A. R. D. J. G. I. B., et al. 2023, , 672, A163, doi: 10.1051/0004-6361/202243572

Oei, M. S. S. L., Hardcastle, M. J., Timmerman, R., et al. 2024, , 633, 537, doi: 10.1038/s41586-024-07879-y

O'Sullivan, S. P., Machalski, J., Van Eck, C. L., et al. 2019, AA, 622, A16, doi: 10.1051/0004-6361/201833832

Paoletti, D., Chluba, J., Finelli, F., & Rubiño-Martín, J. A. 2019, , 484, 185, doi: 10.1093/mnras/sty3521

Paoletti, D., Chluba, J., Finelli, F., & Rubiño-Martín, J. A. 2019, Monthly Notices of the Royal Astronomical Society, 484, 185–195, doi: 10.1093/mnras/sty3521

Paoletti, D., & Finelli, F. 2019, JCAP, 2019, 028, doi: 10.1088/1475-7516/2019/11/028

Penrose, R. 1969, Nuovo Cimento Rivista Serie, 1, 252

Perucho, M. 2019, Galaxies, 7, 70, doi: 10.3390/galaxies7030070

Pian, E., Vacanti, G., Tagliaferri, G., et al. 1997, The Astrophysical Journal, 492, L17, doi: 10.1086/311083

Planck Collaboration, Ade, P. A. R., Aghanim, N., et al. 2016, AA, 594, A19, doi: 10.1051/0004-6361/201525821

Quashnock, J. M., Loeb, A., & Spergel, D. N. 1989, , 344, L49, doi: 10.1086/185528

Ryu, D., Schleicher, D. R. G., Treumann, R. A., Tsagas, C. G., & Widrow, L. M. 2011, Space Science Reviews, 166, 1–35, doi: 10.1007/s11214-011-9839-z

Spurio, M. 2018, Probes of Multimessenger Astrophysics. Charged cosmic rays, neutrinos, γ-rays and gravitational waves, Astronomy and Astrophysics Library (Springer), doi: 10.1007/978-3-319-96854-4

Tavecchio, F., Ghisellini, G., Ghirlanda, G., Foschini, L., & Maraschi, L. 2010, Monthly Notices of the Royal Astronomical Society, 401, 1570–1586, doi: 10.1111/j.1365-2966.2009.15784.x

Tchekhovskoy, A., & Bromberg, O. 2016, Monthly Notices of the Royal Astronomical Society: Letters, 461, L46, doi: 10.1093/mnrasl/slw064

Tjemsland, J., Meyer, M., & Vazza, F. 2024, , 963, 135, doi: 10.3847/1538-4357/ad22dd

Turner, M. S., & Widrow, L. M. 1988, Phys. Rev. D, 37, 2743, doi: 10.1103/PhysRevD.37.2743

van Velzen, S., Falcke, H., Schellart, P., Nierstenhöfer, N., & Kampert, K.-H. 2012, Astronomy amp; Astrophysics, 544, A18, doi: 10.1051/0004-6361/201219389

Vazza, F., Brueggen, M., Gheller, C., et al. 2017, Classical and Quantum Gravity. http://iopscience.iop.org/10.1088/1361-6382/aa8e60

Vazza, F., Gheller, C., Zanetti, F., et al. 2025, , 696, A58, doi: 10.1051/0004-6361/202451709

Vernstrom, T., Heald, G., Vazza, F., et al. 2021, MNRAS, 505, 4178, doi: 10.1093/mnras/stab1301

Vernstrom, T., West, J., Vazza, F., et al. 2023, Science Advances, 9, eade7233, doi: 10.1126/sciadv.ade7233

Widrow, L. M., Ryu, D., Schleicher, D. R. G., et al. 2011, Space Science Reviews, 166, 37–70, doi: 10.1007/s11214-011-9833-5

Willis, A. G., Strom, R. G., & Wilson, A. S. 1974, , 250, 625, doi: 10.1038/250625a0

Wright, M. D. 2015, Physica Medica: European Journal of Medical Physics, 31, 601, doi: 10.1016/j.ejmp.2015.04.003

Yoshida, K., Petropoulou, M., Murase, K., & Oikonomou, F. 2023, The Astrophysical Journal, 954, 194, doi: 10.3847/1538-4357/acea74